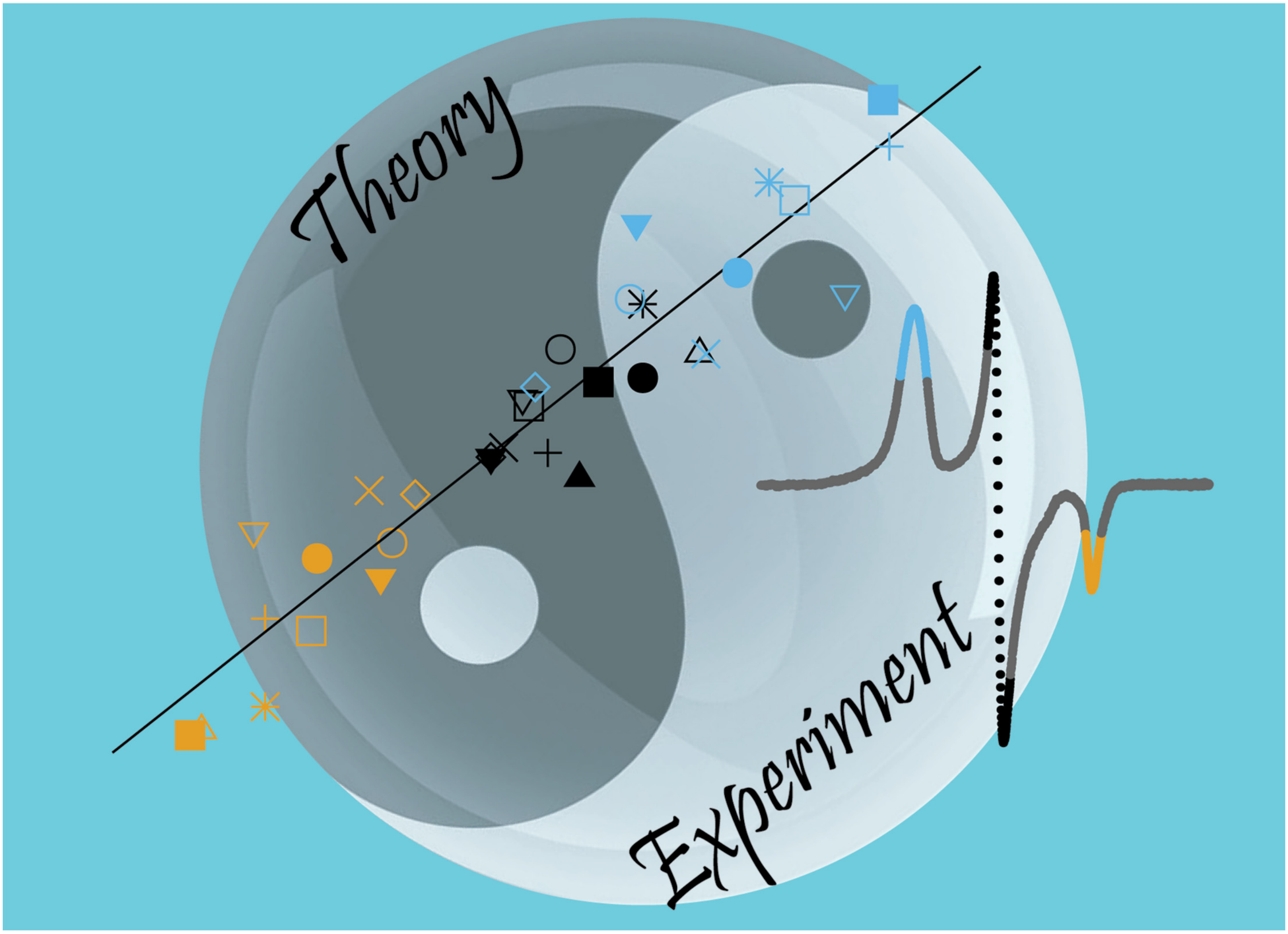

Showcasing research from Professor Pushkar's laboratory, Department of Physics and Astronomy, Purdue University

Multiconfigurational electronic structure calculations explain the role of ligands in *g*-tensor anisotropy for Ru^{III} complexes

Identification of radical intermediates by means of electron paramagnetic resonance benefits from theoretical computation of the EPR parameters such as *g*-tensor and hyperfine splitting. Here, we provide a theoretical analysis for twelve reactive Ru^{III} intermediates catalysing water oxidation, a key reaction in artificial photosynthesis. Using multireference methods, we compute *g*-tensor values and assess the errors against experimental data. Our calculations reproduce previously reported experimental trends, which we explain from a theoretical perspective. Based on our benchmarking we recommend a robust computational protocol.

Image reproduced by permission of Yulia Pushkar from *Phys. Chem. Chem. Phys.*, 2025, **27**, 22937.

As featured in:

See Pavel Pokhilko and Yulia Pushkar, *Phys. Chem. Chem. Phys.*, 2025, **27**, 22937.

PCCP

PAPER

View Article Online
View Journal | View Issue

Cite this: *Phys. Chem. Chem. Phys.*, 2025, **27**, 22937

Received 28th August 2025,
Accepted 6th October 2025

DOI: 10.1039/d5cp03298a

rsc.li/pccp

Multiconfigurational electronic structure calculations explain the role of ligands in *g*-tensor anisotropy for Ru^{III} complexes

Pavel Pokhilko * and Yulia Pushkar *

Identification of radical intermediates by means of electron paramagnetic resonance benefits from the theoretical computation of the EPR parameters such as *g*-tensor and hyperfine splitting. In this work, we provide a theoretical analysis for a dozen reactive Ru^{III} intermediates catalyzing water oxidation, a key reaction in artificial photosynthesis. Using multireference methods, we compute *g*-tensor values and assess the errors against the experimental data. We provide a quantitative analysis of spin–orbit coupling through spinless triplet natural transition orbitals generalizing the El-Sayed–Kanamori rules. We show that the main factor determining *g*-tensor anisotropy is the energy difference between the nearly degenerate 4d-electronic states localized on the Ru^{III} ion. Using natural orbitals, we explain the energy gaps between these states through a ligand-dependent partial charge transfer between Ru and ligands. We show that the energy gaps are strongly affected by the treatment of the weak electron correlation. Our calculations reproduce the previously reported experimental trends, which we now explain from a theoretical perspective. On the basis of our benchmark, we recommend a few modifications of the commonly used computational protocols.

1 Introduction

Electron paramagnetic resonance (EPR) spectroscopy is a powerful tool for investigating reaction mechanisms in solutions,[1,2] on surfaces,[3,4] and in biological systems.[5,6] The unique sensitivity to a chemical environment of radical centers allows one to use EPR techniques to fingerprint reactive transition-metal intermediates in catalytic reactions with 3d and 4d metals, such as V^{IV},[7] Mn^{III},[8,9] Mn^{IV},[9] Fe^{III},[10,11] Fe^{V},[10,12,13] Co^{0},[14] Co^{II},[15] Ni^{I},[14,16] Cu^{II};[17] Mo^{V},[18,19] Nb^{IV},[20,21] Rh^{I},[22] and Rh^{II}.[23,24] Provided by EPR, the *g*-tensors and hyperfine couplings enable characterisation and determination of such species in complicated catalytic cycles.[25]

The rich chemistry of ruthenium complexes is of interest in several fields, ranging from the development of electroluminescence devices[26] to anticancer drugs.[27] Ruthenium catalysts are used for olefin metathesis,[28] hydrogenation of polar bonds,[29] and N_2[30] and C–H bond activation.[31,32] Water oxidation (WO) is another complex reaction facilitated by ruthenium catalysts, which is the focus of mechanistic studies in our group. Since the publication of the first binuclear ruthenium water oxidation catalyst (WOC),[33] many mono and binuclear catalysts have been reported.[34–36] The water oxidation half-reaction involves a transfer of 4 electrons and 4 protons. While there are two main proposed mechanisms[37]—water nucleophilic attack and radical coupling—for many compounds, the mechanistic details are often unclear. Although EPR spectroscopy can detect unstable radical species formed during the catalytic cycle, the correspondence between the specific signal and the specific intermediate is not always straightforward due to the potential presence of multiple species. Predictive quantum chemical calculations can give valuable insights into the electronic structure of such species and their reactivity controlled by the chemical structure of ligands,[38–40] provide estimates of their EPR parameters, and help in the assignments of the EPR signals to specific intermediates.

The majority of previous computational works on ruthenium WOC were focused on mechanistic investigations using density functional theory (DFT) and multiconfigurational methods.[48–53] A few papers have investigated Ru^{III} EPR parameters computationally and theoretically, but only for a few specific compounds.[41,54–56] The nearly degenerate d-orbitals on the Ru^{III} center lead to the nearly degenerate electronic states[54–56] (Fig. 1), described by d^5 configurations. In this work, we systematically study Ru^{III} complexes (Fig. 2), which were previously examined experimentally in our and other groups (Table 1). We theoretically assess the role of ligands in the experimental observables. We describe the electronic structure of these species using complete active space self-consistent

Department of Physics and Astronomy, Purdue University, West Lafayette, Indiana 47907, USA. E-mail: ppokhlk@purdue.edu, ypushkar@purdue.edu

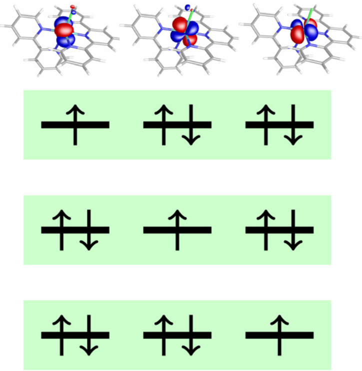

Fig. 1 Nearly degenerate orbitals and leading determinants (in the green boxes) of the nearly degenerate electronic states common for all the considered d^5 complexes.

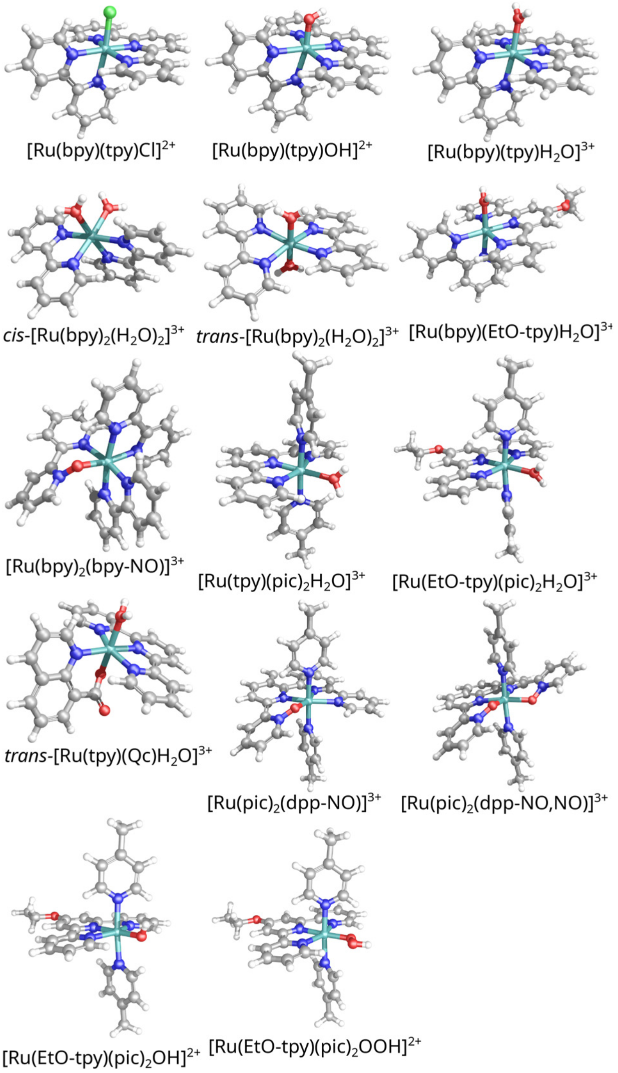

Fig. 2 Ru^{III} complexes studied in this work. The color code is as follows: cyan is for Ru, deep blue is for N, red is for O, gray is for C, green is for Cl, and white is for H.

field (CASSCF) and N-electron valence perturbation theory of the second order (NEVPT2), evaluate and characterize relevant electronic states, and compute *g*-tensors. We provide insights into the origin of these electronic states, their energy separation, the origin of spin–orbit couplings, and the role of electron correlation from several types of natural orbital analyses and quantification of electronic screening. In particular, we show that the larger the partial charge transfer between Ru and ligands is, the larger is the energy separation between the lowest states. The *g*-tensor anisotropy is inversely proportional to the energy gaps of the interacting electronic states, which are influenced by the charge transfer. We reproduced several experimental trends in *g*-factors and explained their origins. We investigated the influence of different factors (geometry, solvent, and electron correlation treatment) on the *g*-tensor estimates and recommend modifications of commonly used computational protocols. We also provide computational evidence which further reinforces the previous assignments of hypothetical Ru^{III} intermediates with modified ligands.

2 Theory

Interaction of a paramagnetic system with the external magnetic field is often described by a phenomenological spin Hamiltonian:

$$H_S = \mu_B \vec{S}\mathbf{g}\vec{B}, \tag{1}$$

where $\vec{S}$ is the spin vector, $\vec{B}$ is the magnetic field, and $\mathbf{g}$ is the *g*-matrix. The principal components of the *g*-matrix, which are accessible from the EPR experiments, are commonly known as *g*-tensor.

The phenomenological definition in eqn (1), however, does not provide an explanation of the origin of the *g*-tensor. Because the *g*-tensor is defined phenomenologically, it is an effective quantity. Despite the simplicity of its definition, the *g*-tensor has contributions from many theoretical terms that are folded in its effective description. These terms may have different relevance for compounds of different nature, explaining why there are many different theoretical approaches for the *g*-tensor evaluation varying in the treatment of electron correlation, relativistic effects, and even the formal definitions of the *g*-tensor,[57] which have been topics of several reviews and book chapters.[58–61] A common viewpoint, which is also applicable in our case, is that the *g*-tensor can be seen as a property of a relativistic Kramers doublet pair within degenerate perturbation theory. There are multiple classes of approaches to calculation of *g*-tensors and relativistic properties in general:

- State-interaction approaches[62–70]
- Quasi-degenerate perturbation theory[60,71–73]
- Response and sum-over-states formalisms[73–77]
- Variational relativistic approaches[78,79]
- Non-collinear generalized Hartree–Fock and Kohn–Sham approaches reconstructing the *g*-tensor from several solutions[78,80,81]

Each of these strategies has pros and cons. For example, variational relativistic approaches can treat very heavy elements but are very computationally expensive to be useful for large

Table 1 Compilation of the experimental studies with the *g*-tensor measurements for all the compounds studied in this work

Specie	Ref.
$[\mathrm{Ru^{III}(bpy)(tpy)Cl}]^{2+}$	41
$[\mathrm{Ru^{III}(bpy)(tpy)OH}]^{2+}$	This work, see Section 3.1 and the Acknowledgments section
$[\mathrm{Ru^{III}(bpy)(tpy)H_2O}]^{3+}$	41
$[\mathrm{Ru^{III}(bpy)(EtO\text{-}tpy)H_2O}]^{3+}$	40
trans-$[\mathrm{Ru^{III}(bpy)_2(H_2O)_2}]^{3+}$	42
cis-$[\mathrm{Ru^{III}(bpy)_2(H_2O)_2}]^{3+}$	42
$[\mathrm{Ru^{III}(bpy)_2(bpy\text{-}NO)}]^{3+}$	43
$[\mathrm{Ru^{III}(tpy)(pic)_2H_2O}]^{3+}$	44
$[\mathrm{Ru^{III}(EtO\text{-}tpy)(pic)_2H_2O}]^{3+}$	44
$[\mathrm{Ru^{III}(EtO\text{-}tpy)(pic)_2OH}]^{2+}$	Hypothetical assignment[45]
$[\mathrm{Ru^{III}(EtO\text{-}tpy)(pic)_2OOH}]^{2+}$	Hypothetical assignment[45]
trans-$[\mathrm{Ru^{III}(tpy)(Qc)H_2O}]^{2+}$	46
$[\mathrm{Ru^{III}(pic)_2(dpp\text{-}NO)}]^{3+}$	Hypothetical assignment[39,47]
$[\mathrm{Ru^{III}(pic)_2(dpp\text{-}NO,NO)}]^{3+}$	Hypothetical assignment[39,47]

molecules. The response and sum-over-states approaches, treating spin–orbit interaction only at the first perturbative order, can be accurate for light elements but yield larger errors when the spin–orbit interaction is larger than the energy gap between electronic states (the perturbative assumption is broken). The approaches using non-collinear SCF solutions rely on the accessibility of these solutions and assume their relatively simple structure, which may not be valid in complicated cases. The state-interaction approaches and quasi-degenerate perturbation theory (which are conceptually equivalent for the perturbative order that we use but different in higher orders) are applicable to the cases of both strong and weak spin–orbit interaction. Their main drawback is in the necessity of converging with respect to the number of interacting states (or the size of the effective Hamiltonian). We show that such a convergence is relatively quick for the considered $\mathrm{Ru^{III}}$ compounds, which allowed us to make meaningful comparisons of computed *g*-factors with the experimental data.

In this work, we capitalize on recent developments[82] factorizing terms in the strongly contracted quasi-degenerate NEVPT2[83,84] that made it applicable to large molecules. Our conclusions, however, should be valid for a number of other correlated methods and comparisons across such methods can be envisioned in the future studies. For example, the target configurations in Fig. 2 can be treated with ionization potential equation-of-motion coupled-cluster methods[85] very well, but their computational cost is too high for complexes of this size.

3 Results

3.1 Experimental results

X-band EPR measurements were performed on an EMX X-band spectrometer equipped with an X-band CW microwave bridge (Bruker, Billerica, MA, USA). During EPR measurements, the sample temperature was maintained at 20 K using a closed-cycle cryostat (ColdEdge Technologies, Allentown, PA, USA). Spectrometer conditions were as follows: microwave frequency 9.47 GHz; field modulation amplitude 25 G at 100 kHz, and microwave power 31.7 mW.

The bulk electrolysis was conducted in a 3-compartment electrochemical cell for the 4 mL of the 0.5 mM $[\mathrm{Ru^{II}(tpy)(bpy)(H_2O)}]^{2+}$ solution in the sodium phosphate buffer (0.1 M NaPi, pH 7) at the potential ∼+0.57 V *vs.* Ag/AgCl for a few hours. For EPR studies of electrolysis samples, samples were prepared by mixing 200 μL of the electrolyzed solution with 20 μL of trifluoroethanol (∼10% final concentration) serving the function of glass forming agent to avoid ice crystallite formation and prevent the EPR broadening by dipole–dipole interaction. The final solution was quickly transferred into the EPR tube where it was frozen within 30 seconds in liquid N_2. The experiment was repeated 3 times and the same EPR spectrum was observed in all experiments. We show the plot with the EPR spectrum in Fig. S1 in the SI.

3.2 Computational details

3.2.1 Active space. We executed CASSCF calculations using the following setup. First, we converged restricted Hartree–Fock calculations for the reduced $\mathrm{Ru^{II}}$ complexes, which gave reliable initial orbitals. Then we used the atomic valence active space (AVAS) procedure[86] to construct initial active spaces containing 4d Ru orbitals for $\mathrm{Ru^{II}}$ and removed one electron from it, which generated the initial active spaces for the target $\mathrm{Ru^{III}}$ complexes. For all the considered complexes, this procedure led to the active spaces with 7 orbitals and 9 electrons, which we denote as CAS(9e,7o). We tested larger active spaces based on AVAS from the 4d Ru orbitals and p_x, p_y, or p_z components on N and Cl (or O) from ligands directly coordinated with Ru. We considered only the p components pointing toward Ru. The additionally captured orbitals in the large active space contributed only to the weak electron correlation (the occupation numbers are bigger than 1.98). Such occupation numbers deteriorate CASSCF convergence and may also lead to an imbalanced treatment of the dynamic correlation. Therefore, we conducted all the calculations reported here with CAS(9e,7o), which is sufficient for capturing local *g*-tensor physics qualitatively, as shown in the sections below. To converge the CASSCF iterations, we used the perturbative super-CI approach[87] for calculations performed with Orca 6.0.1[88] and the co-iterative augmented Hessian method[89,90] for calculations performed with PySCF.[91,92]

3.2.2 Geometries. In our preliminary calculations, we observed a substantial dependence of *g*-tensors on the used geometry. We investigated it further and considered three types of optimized geometries. First, we used the previously reported B3LYP/DGDZVP/6-31G* geometries with explicit water from ref. 41 for $[\mathrm{Ru^{III}(bpy)(tpy)X}]^{(3-n)+}\cdot 2\mathrm{H_2O}$ for X = $\mathrm{H_2O}$ and $\mathrm{OH^-}$. We optimized the case X = $\mathrm{Cl^-}$ in the same way with the same basis sets[93–95] using Gaussian 09,[96] solely for comparison purposes. The M06-L geometries of *cis*- and *trans*-$[\mathrm{Ru^{III}(bpy)_2(H_2O)_2}]^{3+}$ were taken from ref. 42.

Second, using the geomopt module of PySCF[91] and PyBerny[97] as an optimizer, we optimized the geometries of the lowest doublet state of the complexes without inclusion of the explicit water using SA-CASSCF(9e,7o)[98] averaged over three nearly-degenerate doublet states with the cc-pVTZ basis set[99,100] on light atoms (H, C, O, N, Cl) and def2-TZVPP basis set[101,102] on Ru with the corresponding effective core potential (ECP). We used the resolution-of-identity (RI) approximation with cc-pVTZ-jkfit[103] and def2-TZVPP-jkfit[104] auxiliary basis sets to reduce memory footprint and speed up large calculations. To accelerate the CASSCF geometry optimization, we locally modified the source code and replaced the conjugate gradient linear solver (scipy.sparse.linalg.cg) for the orbital response equations with the LGMRES solver[105,106] (scipy.sparse.linalg.lgmres) and expanded the Krylov subspace using vectors from the previous geometries. This approach, on average, reduced the number of iterations from about 50 (which did not always converge) to about 3.

Third, to optimize positions of water molecules in the selected clusters, we froze the SA-CASSCF geometry of the complex, placed water molecules forming hydrogen bonds with X ligands, and optimized water positions with r^{2}SCAN functional[107] and cc-pVTZ basis set again within the RIJK approximation (with cc-pVTZ-jkfit auxiliary basis) using Orca 6.0.1.[88] This scheme allowed us to optimize the positions of water molecules efficiently in just very few iterations.

The Cartesian coordinates of all the used geometries are listed in the SI.

3.2.3 Single-point *g*-tensor calculations. The single-point SA-CASSCF(9e,7o) and strongly contracted Van Vleck QD-NEVPT2[83,84] calculations were performed with Orca 6.0.1 using spin-free exact two-component (SFX2C) formalism (incorporated variationally)[108,109] and with cc-pVTZ basis on O, N, Cl, C, cc-pVDZ on H, and ANO-RCC-VTZP[110] on Ru. We used two types of state averaging: over the three lowest doublet states and over the lowest three doublets and two quartets. We used the RI approximation with cc-pVTZ-jkfit auxiliary basis set on light atoms and with an automatically generated auxiliary basis set on Ru with the AutoAux procedure.[111] The core electrons were frozen using the default treatment in Orca 6.0.1. The spin–orbit interaction was treated by means of X2C-RI-SOMF(1X) approximation,[112,113] where the relativistic Coulomb term was evaluated with RI, with quasidegenerate perturbation theory (which is equivalent in this order to the state interaction approach). The relativistic picture-change effects were included in the spin–orbit calculation.

3.2.4 Analysis. We wrote scripts generating natural orbitals and triplet spinless natural transition orbitals[114] from the SA-CASSCF using the PySCF code base. Then we prepared orbitals using the Molden printer from PySCF, plotted orbitals in Gabedit 2.5.1[115] with an isovalue of 0.050, and rendered orbitals with POV-Ray 3.7.0.[116]

3.3 Numerical results

3.3.1 Geometries. DFT methods have known limitations when applied to strongly correlated systems, such as a qualitatively incorrect description of strong electron correlation, a presence of multiple solutions, and spin contamination. The charge and spin delocalization errors can lead to an incorrect description even for weakly correlated systems and reactions, including reaction products,[117] reaction intermediates,[118] and solvation clusters.[119] Given that the electronic states are nearly degenerate and that the pseudo-Jahn–Teller effect is likely to occur, we optimized the geometries of all the considered compounds with SA-CASSCF and compared them with the DFT geometries.

The structures optimized with SA-CASSCF are often symmetric with the following point groups: C_s for $[\mathrm{Ru^{III}(bpy)(tpy)X}]^{3-n+}$, D_2 for *trans*-$[\mathrm{Ru^{III}(bpy)_2(H_2O)_2}]^{3+}$, C_2 for *cis*-$[\mathrm{Ru^{III}(bpy)_2(H_2O)_2}]^{3+}$ and $[\mathrm{Ru^{III}(pic)_2(dpp\text{-}NO,NO)}]^{3+}$. The reported DFT optimized structures slightly deviate from the symmetric geometries. We compare the selected bond lengths for the considered species in Tables 2 and 3 and deposit the Cartesian coordinates of the optimized structures in Å in the zip archive in the SI.

3.3.2 Excitation energies. For the further analysis, we evaluated excitation energies between nearly degenerate electronic

Table 2 Bond lengths (Å) in $[\mathrm{Ru^{III}(bpy)(tpy)Cl}]^{2+}$, $[\mathrm{Ru^{III}(bpy)(tpy)OH}]^{2+}$, and $[\mathrm{Ru^{III}(bpy)(tpy)H_2O}]^{3+}$

Cl	DFT[a]	CASSCF	OH^-	DFT[a]	CASSCF	H_2O	DFT[a]	CASSCF
Ru–Cl	2.394	2.341	Ru–O	1.947	1.921	Ru–O	2.085	2.224
Ru–N1 (tpy)	2.127	2.132	Ru–N1 (tpy)	2.139	2.144	Ru–N1 (tpy)	2.123	2.127
Ru–N2 (tpy)	2.042	2.030	Ru–N2 (tpy)	2.024	2.035	Ru–N2 (tpy)	2.040	2.044
Ru–N3 (tpy)	2.127	2.132	Ru–N3 (tpy)	2.139	2.144	Ru–N3 (tpy)	2.127	2.127
Ru–N4 (bpy)	2.113	2.161	Ru–N4 (bpy)	2.164	2.205	Ru–N4 (bpy)	2.097	2.082
Ru–N5 (bpy)	2.140	2.165	Ru–N5 (bpy)	2.131	2.147	Ru–N5 (bpy)	2.131	2.120

[a] From the structure with the explicit water present.

Table 3 Bond lengths (Å) in *cis*-, *trans*-$[\mathrm{Ru^{III}(bpy)_2(H_2O)_2}]^{3+}$, and $[\mathrm{Ru^{III}(tpy)(pic)_2H_2O}]^{3+}$

cis	DFT	CASSCF	*trans*	DFT	CASSCF	$[\mathrm{Ru^{III}(tpy)(pic)_2H_2O}]^{3+}$	CASSCF
Ru–O1	2.176	2.178	Ru–O1	2.081	2.080	Ru–O	2.246
Ru–O2	2.201	2.178	Ru–O2	2.081	2.080	Ru–N1 (tpy)	1.993
Ru–N1	2.095	2.122	Ru–N1	2.110	2.146	Ru–N2 (tpy)	2.122
Ru–N2	2.027	2.063	Ru–N2	2.122	2.154	Ru–N3 (tpy)	2.116
Ru–N3	2.031	2.063	Ru–N3	2.110	2.146	Ru–N4 (pic)	2.146
Ru–N4	2.094	2.122	Ru–N4	2.123	2.154	Ru–N5 (pic)	2.168

Table 4 SA-CASSCF(9e,7o), diagonal NEVPT2, and QD-NEVPT2 excitation energies, cm^{-1} (eV), evaluated at the lowest doublet state geometry optimized with SA-CASSCF(9e,7o). The state averaging is performed over the lowest 3 doublets. The QD-NEVPT2 effective Hamiltonian is constructed from 3 doublets

	SA-CASSCF		NEVPT2		QD-NEVPT2	
$[Ru^{III}(bpy)(tpy)Cl]^{2+}$	1486	(0.184)	1799	(0.223)	1809	(0.224)
	3374	(0.418)	4129	(0.512)	4149	(0.514)
$[Ru^{III}(bpy)(tpy)OH]^{2+}$	2920	(0.362)	4535	(0.562)	4542	(0.563)
	6039	(0.749)	7750	(0.961)	7763	(0.963)
$[Ru^{III}(bpy)(tpy)H_2O]^{3+}$	1894	(0.235)	2077	(0.258)	2078	(0.258)
	2313	(0.287)	2200	(0.273)	2202	(0.273)
$[Ru^{III}(bpy)(EtO\text{-}tpy)H_2O]^{3+}$	1367	(0.169)	1234	(0.153)	1235	(0.153)
	2402	(0.298)	2262	(0.280)	2265	(0.281)
trans-$[Ru^{III}(bpy)_2(H_2O)_2]^{3+}$	3479	(0.431)	4483	(0.556)	4325	(0.536)
	3560	(0.441)	4492	(0.557)	4650	(0.577)
cis-$[Ru^{III}(bpy)_2(H_2O)_2]^{3+}$	2790	(0.346)	3226	(0.400)	3243	(0.402)
	3542	(0.439)	3914	(0.485)	3946	(0.489)
$[Ru^{III}(bpy)_2(bpy\text{-}NO)]^{3+}$	1872	(0.232)	2531	(0.314)	2540	(0.315)
	2911	(0.361)	3663	(0.454)	3677	(0.456)
$[Ru^{III}(tpy)(pic)_2H_2O]^{3+}$	1495	(0.185)	1688	(0.209)	1686	(0.209)
	2307	(0.286)	2407	(0.298)	2410	(0.299)
$[Ru^{III}(EtO\text{-}tpy)(pic)_2H_2O]^{3+}$	739	(0.092)	1086	(0.135)	1086	(0.135)
	2180	(0.270)	2553	(0.317)	2554	(0.317)
$[Ru^{III}(EtO\text{-}tpy)(pic)_2OH]^{2+}$	2649	(0.328)	4285	(0.531)	4287	(0.531)
	4727	(0.586)	6652	(0.825)	6653	(0.825)
$[Ru^{III}(EtO\text{-}tpy)(pic)_2OOH]^{2+}$	2850	(0.353)	4225	(0.524)	4235	(0.525)
	3218	(0.399)	4676	(0.580)	4681	(0.580)
trans-$[Ru^{III}(tpy)(Qc)H_2O]^{2+}$	2434	(0.302)	3501	(0.434)	3500	(0.434)
	3559	(0.441)	5128	(0.636)	5136	(0.637)
$[Ru^{III}(pic)_2(dpp\text{-}NO)]^{3+}$	2089	(0.259)	3127	(0.388)	3126	(0.388)
	3655	(0.453)	4626	(0.574)	4637	(0.575)
$[Ru^{III}(pic)_2(dpp\text{-}NO,NO)]^{3+}$	4745	(0.588)	6442	(0.799)	6453	(0.800)
	5252	(0.651)	6515	(0.808)	6521	(0.808)

states for all the considered species at their optimized SA-CASSCF structures (Table 4). The excitation energies are sensitive to the correlation treatment. The excitation energies found from CASSCF and QD-NEVPT2 differ by 0.1–0.3 eV, which are within typical errors for excitation energies. However, since the states are nearly degenerate, the relative changes in excitation energies can be as large as 1.5 times. For most systems, the inclusion of dynamic correlation increases the excitation energies, which is likely due to electronic screening (see also Section 4.1). The only systems for which the excitation energies slightly decrease are $[Ru^{III}(bpy)(tpy)H_2O]^{3+}$ and $[Ru^{III}(bpy)(EtO\text{-}tpy)H_2O]^{3+}$. The changes in excitation energies have a significant influence on the *g*-tensor estimates (Table 5), which we analyze in Section 4.3. We continue the discussion about excitation energies, their origins, and trends in Section 4.1.

3.3.3 *g*-tensor calculations. In the spin–orbit-diabatic representation, the *g*-tensor is expressed through the state interaction with a number of interacting excited states or through the effective Hamiltonians of increasing dimensions. It is important to test the convergence of the *g*-tensor with respect to the number of excited states. Tables S4–S6 in the SI show the convergence of the *g*-tensor for $[Ru^{III}(bpy)(tpy)Cl]^{2+}$. While the excited states are much higher in energy, both excited doublet and quartet states contribute to the *g*-tensor estimates. We noticed that 20 doublet and 8 quartet states included in the evaluation of the *g*-tensors are sufficient to converge the estimates with respect to the number of the excited states. We incorporated this treatment for all the systems we report here except $[Ru^{III}(bpy)(tpy)OH]^{2+}$, for which we had to reduce the size of the effective Hamiltonian to 10 doublets and 2 quartets due to negative denominators (pseudo-intruder states) in NEVPT2.

In previous studies using CASSCF and post-CASSCF methods for *g*-tensor evaluation, different orbitals were used, such as state-specific orbitals,[120] and state-averaging over several or large number of electronic states.[65,73] In our case, however,

Table 5 Theoretical g-tensor components at the SA-CASSCF structures and experimental estimates. In all the cases, we used 20 doublet and 8 quartet states to evaluate components of the g-tensors from the effective Hamiltonians. The references of the experimental estimates are listed in Table 1

	Averaging over 3d2q			Averaging over 3d			
	CASSCF	NEVPT2	QD-NEVPT2	CASSCF	NEVPT2	QD-NEVPT2	Exp
$[\mathrm{Ru^{III}(bpy)(tpy)Cl}]^{2+}$	1.074	1.290	1.316	1.237	1.439	1.449	1.66
	2.286	2.287	2.271	2.193	2.202	2.214	2.25
	3.318	3.202	3.151	3.204	3.100	3.075	2.79
$[\mathrm{Ru^{III}(bpy)(tpy)OH}]^{2+}$	1.718	1.826	1.827	1.769[a]	1.881[a]	1.878[a]	1.84
	2.227	2.228	2.243	2.216	2.213	2.229	2.18
	2.798	2.575	2.528	2.727	2.496	2.492	2.50
$[\mathrm{Ru^{III}(bpy)(tpy)H_2O}]^{3+}$	1.007	1.025	1.051	1.241	1.264	1.154	1.66
	2.700	2.722	2.683	2.489	2.565	2.632	2.40
	3.037	3.002	2.968	2.973	2.896	2.974	2.60
$[\mathrm{Ru^{III}(bpy)(EtO\text{-}tpy)H_2O}]^{3+}$	0.945	0.804	0.852	1.020	0.902	1.058	1.53
	2.413	2.336	2.362	2.262	2.223	2.413	2.33
	3.291	3.387	3.278	3.232	3.286	3.206	2.78
trans-$[\mathrm{Ru^{III}(bpy)_2(H_2O)_2}]^{3+}$	1.537	1.655	1.667	1.555	1.700	1.703	1.88
	2.532	2.542	2.528	2.587	2.513	2.505	2.27
	2.877	2.672	2.638	2.832	2.652	2.646	2.38
cis-$[\mathrm{Ru^{III}(bpy)_2(H_2O)_2}]^{3+}$	1.356	1.490	1.505	1.607	1.659	1.651	1.75
	2.539	2.522	2.503	2.434	2.429	2.425	2.40
	3.026	2.908	2.860	2.815	2.710	2.720	2.55
$[\mathrm{Ru^{III}(bpy)_2(bpy\text{-}NO)}]^{3+}$	1.177	1.408	1.443	1.054	1.376	1.408	1.74
	2.381	2.382	2.340	2.374	2.386	2.345	2.22
	3.105	2.947	2.898	3.166	2.971	2.924	2.64
$[\mathrm{Ru^{III}(tpy)(pic)_2H_2O}]^{3+}$	0.238	0.391	0.451	0.751	0.896	1.080	1.55
	2.405	2.536	2.496	2.445	2.498	2.497	
	3.234	3.134	3.085	2.977	2.916	2.880	2.49
$[\mathrm{Ru^{III}(EtO\text{-}tpy)(pic)_2H_2O}]^{3+}$	0.487	0.748	0.619	0.286	0.736	0.589	
	2.312	2.375	2.156	2.172	2.373	2.148	2.3
	3.267	3.219	3.309	3.317	3.198	3.302	2.62
$[\mathrm{Ru^{III}(EtO\text{-}tpy)(pic)_2OH}]^{2+}$	1.818	1.856	1.882	1.634	1.851	1.858	
	2.237	2.191	2.164	2.318	2.277	2.283	
	2.528	2.449	2.311	2.913	2.600	2.542	
$[\mathrm{Ru^{III}(EtO\text{-}tpy)(pic)_2OOH}]^{2+}$	1.641	1.782	1.780	1.533	1.779	1.777	
	2.474	2.409	2.430	2.530	2.412	2.431	
	2.781	2.617	2.538	2.826	2.606	2.540	
trans-$[\mathrm{Ru^{III}(tpy)(Qc)H_2O}]^{2+}$	1.584	1.739	1.750	1.477	1.732	1.736	1.64
	2.378	2.339	2.325	2.413	2.342	2.362	2.21
	2.835	2.669	2.632	2.949	2.728	2.656	2.72
$[\mathrm{Ru^{III}(pic)_2(dpp\text{-}NO)}]^{3+}$	1.317	1.563	1.582	1.261	1.573	1.580	1.86
	2.153	2.234	2.208	2.163	2.219	2.196	2.16
	3.204	2.909	2.871	3.194	2.874	2.853	2.39
$[\mathrm{Ru^{III}(pic)_2(dpp\text{-}NO,NO)}]^{3+}$	1.793	1.864	1.864	1.778	1.867	1.865	1.92
	2.265	2.224	2.196	2.276	2.227	2.202	2.16
	2.542	2.405	2.398	2.575	2.404	2.399	2.23

[a] Due to negative denominators, a reduced size of the effective Hamiltonian was used.

the contributing states have a different significance. The three lowest doublet states have the biggest impact on the g-tensor components. Performing state averaging over a larger number of states may deteriorate the quality of these lowest doublet states and the g-tensor estimates. To test it, we report estimates obtained with two different state averaging schemes: over three doublets and two quartets and only over three doublets, which we show in Table 5 at the SA-CASSCF geometries. We represent the same results graphically in Fig. 3.

Since the g-tensor measurements are performed in solutions of these species, one may expect some influence of the solvent as well as different geometric distortions. We tested the sensitivity of the g-tensor estimates on the geometries and the presence of explicit water molecules in Tables S7–S9 in the SI,

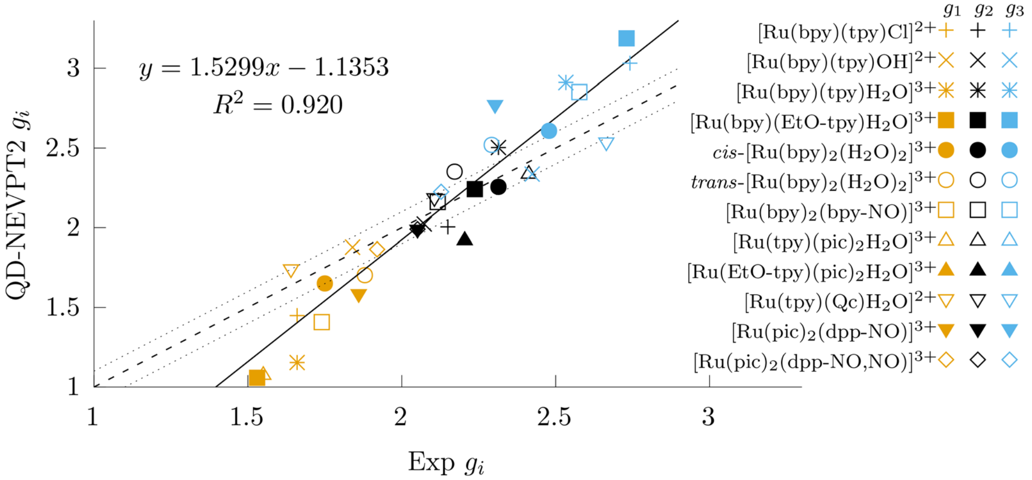

Fig. 3 Correlation between the experimental measurements and QD-NEVPT2 estimates (from SA-CASSCF(9e,7o) averaged over 3 doublets, SA-CASSCF geometry in vacuum). All the estimates are taken from Table 5. The black solid line is the least-squared fit (excluding the hypothetical intermediates). The optimal parameters of the fit and the coefficient of determination (R^2) are shown on the graph. The dashed line represents the ideal agreement between theory and experimental measurements. The dotted lines denote the ideal agreement ±0.1, which is the approximated experimental uncertainty.

showing the computed *g*-tensors with CASSCF, NEVPT2 (CASSCF with NEVPT2 diagonal energies), and QD-NEVPT2. We discuss the observed trends in Section 4.3.

4 Analysis and discussion

4.1 Structure of relevant electronic states

Spin-averaged natural orbitals (SA-NOs, also simply called natural orbitals), defined as eigenvectors of the spin-averaged density matrix of the individual electronic state ($\gamma_{\alpha\alpha} + \gamma_{\beta\beta}$), are a convenient way to gain insights into magnetic interactions in molecules[121–123] and solids.[124] Spin-averaged natural orbitals (Fig. 4 and Fig. S2 and S3 in the SI) reveal the origin of the near-degeneracy of the doublet states. For every species, shapes and occupations of bonding and antibonding SA-NOs are very similar for every nearly-degenerate doublet state. The only difference is in the location of the natural orbitals occupied by an unpaired electron, corresponding to different non-bonding d-orbitals almost fully localized on Ru. These non-bonding orbitals almost do not mix with the orbitals from the ligands, which explains why these orbitals are nearly degenerate and why the corresponding many-electron wave functions are also nearly degenerate.

The similarities and differences of SA-NOs between different species provide insights into the role of ligands. For example, anionic ligands X = Cl^- and OH^- produce natural orbitals of similar shapes and occupancies, meaning that the structure of electron correlation in these species is also similar. However, the difference comes from the small but noticeable mixing of p-orbitals on X with the non-bonding d-orbitals on Ru. For OH^-, this mixing is different for different non-bonding d-orbitals, which is sufficient to noticeably change the energies of the corresponding doublet states. This explains why the excitation energies of $[Ru^{III}(bpy)(tpy)OH]^{2+}$ in Table 4 are much higher than the excitation energies of $[Ru^{III}(bpy)(tpy)Cl]^{2+}$.

The structure of SA-NOs for $[Ru^{III}(bpy)(tpy)H_2O]^{3+}$ is slightly different from $[Ru^{III}(bpy)(tpy)OH]^{2+}$ and $[Ru^{III}(bpy)(tpy)Cl]^{2+}$. This is not surprising because of the different charge, the different Ru–O bond strengths, and the different bond lengths. In particular, the participation of orbitals from the H_2O ligand is very small even for nearly unoccupied and nearly doubly occupied active-space orbitals. The amount of mixing of the H_2O orbitals with the non-bonding d-orbitals on Ru is comparable with Cl^-, which explains why the excitation energies of $[Ru^{III}(bpy)(tpy)H_2O]^{3+}$ are also small.

We show the SA-NOs for *cis* and *trans*-$[Ru^{III}(bpy)_2(H_2O)_2]^{3+}$ in Fig. S4 and S5 in the SI. Similarly to the SA-NOs for $[Ru^{III}(bpy)(tpy)H_2O]^{3+}$, nearly unoccupied and nearly doubly occupied orbitals describe mostly correlation along Ru–N bonds and contain only small contributions from water ligands. However, the key distinction between these species lies in the contribution of water ligands to the singly occupied SA-NO in the ground state and excited state. The singly occupied SA-NO for the *trans* isomer has the largest contribution from water, followed by the *cis* isomer, and then by $[Ru^{III}(bpy)(tpy)H_2O]^{3+}$. This series is consistent with the decrease in excitation energies from the ground state to the first and the second excited doublet, which is fully consistent with explanations for other species.

Similarly to $[Ru^{III}(bpy)(tpy)H_2O]^{3+}$, the open-shell SA-NOs for $[Ru^{III}(tpy)(pic)_2H_2O]^{3+}$ (Fig. S6) have only small contributions from ligands. The excitation energies to the first and the second excited doublet states are also small, which preserves the trend described above. The ethoxy derivatives, $[Ru^{III}(bpy)(EtO\text{-}tpy)H_2O]^{3+}$ and $[Ru^{III}(EtO\text{-}tpy)(pic)_2H_2O]^{3+}$ (Fig. S7 and S10 in the SI), also have only small contributions from the water ligand. However, both ethoxy derivatives have additional contributions from the

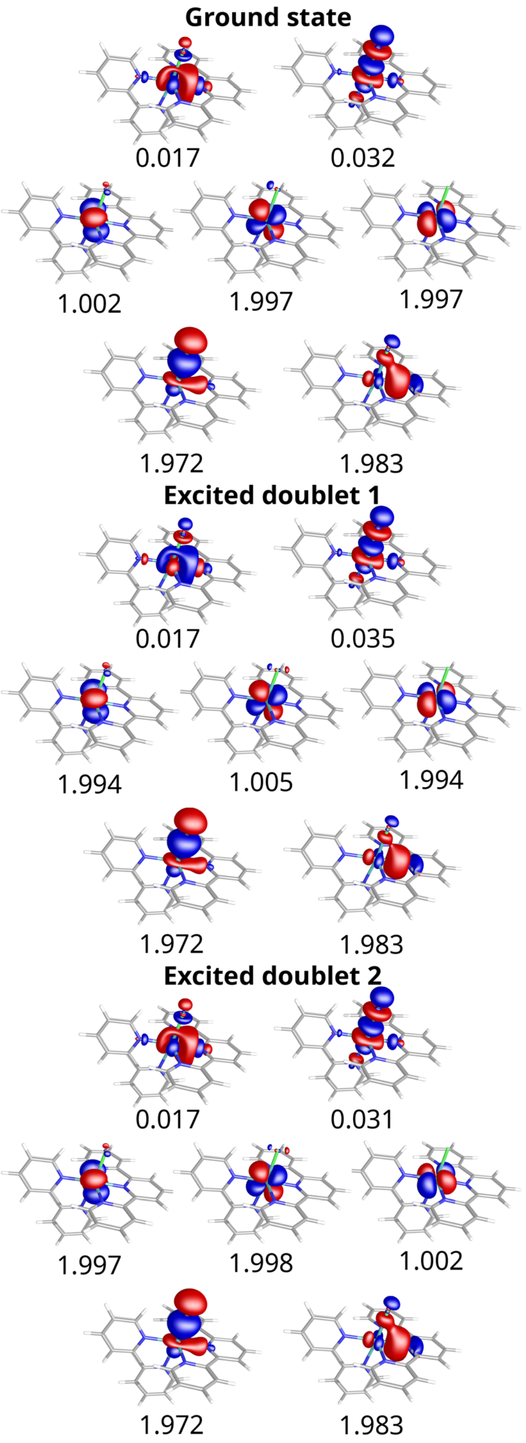

Fig. 4 Spin-averaged natural orbitals of individual states found with SA-CASSCF(9e,7o) shown for $[Ru^{III}(bpy)(tpy)Cl]^{2+}$. The occupations of every natural orbital are shown below the orbitals.

central nitrogen of tpy. The ethoxy derivatives have smaller excitation energies to the first excited doublet than the parent compounds. While the exact origin of this change in excitation energies is unclear, the trends observed in calculations are consistent with the experimental trends in *g*-tensors (Section 4.3).

$[Ru^{III}(bpy)_2(bpy\text{-}NO)]^{3+}$ and *trans*-$[Ru^{III}(tpy)(Qc)H_2O]^{2+}$ (Fig. S11 and S12 in the SI) share many similarities with other systems. The contribution from the water ligand into the open-shell SA-NOs is small, but the contribution from the *N*-oxide and carboxyl oxygen's p-orbitals is noticeable. The excitation energies to the first and the second excited doublet states are smaller than in $[Ru^{III}(bpy)(tpy)OH]^{2+}$. A potential explanation is the smaller local charge on oxygen reducing its π-donating properties. The SA-NOs for $[Ru^{III}(pic)_2(dpp\text{-}NO)]^{3+}$ and $[Ru^{III}(pic)_2(dpp\text{-}NO,NO)]^{3+}$ are similar to $[Ru^{III}(bpy)_2(bpy\text{-}NO)]^{3+}$. The excitation energies of $[Ru^{III}(pic)_2(dpp\text{-}NO)]^{3+}$ and $[Ru^{III}(bpy)_2(bpy\text{-}NO)]^{3+}$ are close. The excitation energies of $[Ru^{III}(pic)_2(dpp\text{-}NO,NO)]^{3+}$ are almost twice bigger than in $[Ru^{III}(pic)_2(dpp\text{-}NO)]^{3+}$, which can be explained through the presence of two Ru–O bonds with ligand mixing in the SA-NOs.

The first excitation energies of $[Ru^{III}(bpy)(tpy)OH]^{2+}$ and $[Ru^{III}(EtO\text{-}tpy)(pic)_2OH]^{2+}$ are close, which is consistent with very similar shapes of SA-NOs and similar mixtures of oxygen into SA-NOs. The excitation energies to the second excited doublet states are somewhat different, which is again consistent with different orientations of the corresponding SA-NOs (in plane with tpy or perpendicular to it). Different orientations of SA-NOs are expected because of the different locations of the hydroxo ligand and the oxygen's lone pair. The SA-NOs for $[Ru^{III}(EtO\text{-}tpy)(pic)_2OH]^{2+}$ and $[Ru^{III}(EtO\text{-}tpy)(pic)_2OOH]^{2+}$ are similar; however, the ordering of the corresponding doublet states is different—the ground and the first excited doublet states are swapped. This swapping can be explained through different pic-Ru–O–X dihedral angles that are responsible for an orientation of the oxygen's lone pair that is mixed with the ruthenium's d-orbitals. The first excitation energies are close, but the second excitation energies are quite different.

SA-NOs can explain the role of the dynamic correlation. The biggest changes in the excitation energies due to the dynamic correlation captured by NEVPT2 are for the systems where the oxygen's p-orbitals are partly mixed with the open-shell non-bonding orbitals on Ru. In the localized description, this corresponds to a partial charge transfer between oxygen and Ru. The phenomenon of such a partial charge transfer for magnetic states is especially well-known for superexchange.[124–126] One of us showed that bubble Feynman diagrams, describing electronic screening, lead to a renormalization of interactions, stabilize the charge-transfer contributions, and substantially improve the estimates of the effective exchange couplings in both molecules and solids.[122,123,127,128] Likely, the same is true for the excitation energies in Ru^{III}–O complexes. Electronic screening enhances the charge transfer for the states where it is already present, increasing the differences in both one- and two-particle density matrices between different states, hence increasing the energy differences.

To confirm the origin of spin–orbit coupling, we analyzed the spinless triplet density matrix introduced by one of us previously,[66,114] which generalizes the concept of natural transition orbitals[129–131] to arbitrary transitions between multiplets. The idea lies in the application of the Wigner–Eckart theorem to the triplet spin-tensor excitation operators, which are defined as

$$\hat{T}^{1,1}_{pq} = -a^{\dagger}_{p\alpha}a_{q\beta}, \qquad (2)$$

$$\hat{T}^{1,0}_{pq} = \frac{1}{\sqrt{2}}\left(a^{\dagger}_{p\alpha}a_{q\alpha} - a^{\dagger}_{p\beta}a_{q\beta}\right), \qquad (3)$$

$$\hat{T}^{1,-1}_{pq} = a^{\dagger}_{p\beta}a_{q\alpha}, \qquad (4)$$

where a and $a^{\dagger}$ are the annihilation and creation operators, respectively. By the Wigner–Eckart theorem, the matrix elements of these spin-tensor operators are proportional to the Clebsh–Gordan coefficients. The reduced matrix element, which is exactly the same for states with any spin projections, is found as

$$u^{1,\cdot}_{kl} = \langle JS\|\hat{T}^{1,\cdot}_{kl}\|IS'\rangle = \langle JSM|\hat{T}^{1,m}_{kl}|IS'M'\rangle/\langle S'M';1m|SM\rangle, \qquad (5)$$

where S, S' are the total spins, M, M' are the spin projections, and $u^{1,\cdot}_{kl}$ is the reduced spinless triplet transition density matrix. The singular-value decomposition of $u^{1,\cdot}_{kl}$ gives the spinless triplet natural transition orbitals, which represent it in a compact way. As a result, any transition triplet property can be represented through the corresponding spinless triplet NTO pairs:

$$\left\langle JS\middle\|\hat{A}^{1,\cdot}\middle\|IS'\right\rangle = \sum_{kl} A^{1,\cdot}_{kl}u^{1,\cdot}_{kl} = \sum_{q} A^{1,\cdot}_{p_q h_q}\sigma_q, \qquad (6)$$

where A is an arbitrary one-particle triplet operator, σ_q is the q-th singular value, and p_q and h_q are the q-th spinless triplet NTO pair, and $A^{1,\cdot}_{p_q h_q}$ is the integral over the NTO pairs for the reduced matrix element. The full set of matrix elements for any transitions between the components of the multiplets can be easily recovered through the application of the Wigner–Eckart theorem.

For all the transitions between the nearly degenerate doublet states in all the considered compounds, only one singular value is large (above 1), while the remaining singular values are by two orders of magnitude smaller. We show the leading spinless triplet NTO pairs for the transitions in $[\mathrm{Ru^{III}(bpy)(tpy)Cl}]^{2+}$ and $[\mathrm{Ru^{III}(bpy)(tpy)OH}]^{2+}$ in Fig. 5. The shapes of the spinless triplet NTOs are very close to the corresponding singly occupied SA-NOs. The spin–orbit operator has a local nature (in the Breit–Pauli form, it has a cubic denominator). The transitions are strongly localized on Ru, which makes the radial part of the spin–orbit integral over the spinless NTOs large. The strong localization of the NTO pairs also allows one to consider these transitions through the approximate local selection rules. The NTO orbitals correspond to $Y_{2,-2}$, $Y_{2,-1}$, $Y_{2,1}$ real solid harmonics in the SI of ref. 114. The corresponding angular momentum matrix elements for L_x, L_y, and L_z are $\pm i$ (atomic units), which makes the angular part of the spin–orbit integral over NTOs large. As a result, the one-electron spin–orbit coupling matrix elements between the nearly degenerate doublet states are large. The essentially one-electron nature of the transitions makes the spin–orbit mean-field approximation accurate. Finally, the localized one-electron nature of the transitions justified the local treatment of the exchange part of the SOMF approximation that we deployed in our calculations of the *g*-tensors.

4.2 Geometries

The average deviations of the Ru–ligand bond lengths between SA-CASSCF and B3LYP (Table 2) are 0.025 Å, 0.017 Å, and 0.024 Å for $[\mathrm{Ru^{III}(bpy)(tpy)Cl}]^{2+}$, $[\mathrm{Ru^{III}(bpy)(tpy)OH}]^{2+}$, and $[\mathrm{Ru^{III}(bpy)(tpy)H_2O}]^{3+}$, respectively. These deviations are comparable with the previously reported average deviation of the Ru–ligand bond lengths between CASSCF and B3LYP for *trans*-$[\mathrm{RuCl_4(NO)}(1H\text{-indazole})]^{-}$, which is 0.020 Å.[132] The biggest deviations in Table 2 are for the following bonds: Ru–Cl (0.053 Å), Ru–N4 (0.048 and 0.041 Å), and Ru–O (0.139 Å). The Ru–Cl bond length from SA-CASSCF (2.341 Å) is comparable with Ru–Cl bond lengths in $[\mathrm{Ru(bpy)_2Cl_2}]\mathrm{Cl}$ (2.321 and 2.328 Å) found from the crystal structure.[133] This agreement is not surprising because the active space includes both bonding and antibonding orbitals along the Ru–Cl bond. Orbitals can also provide insight into the difference of the geometries between different methods. The singly occupied SA-NO for the B3LYP Kohn–Sham determinant (Fig. 6) shows the natural orbital similar to the SA-CASSCF one, but with a substantial involvement of Cl p-orbitals. The antibonding combination of d and p-orbitals effectively reduces the bond order resulting in a bigger bond length. This effect is likely a manifestation of the charge and spin delocalization error.

The nature of the coordinating ligand determines the Ru–O bond length. DFT and SA-CASSCF estimates of the Ru–OH bond lengths are in agreement. They are also close to the

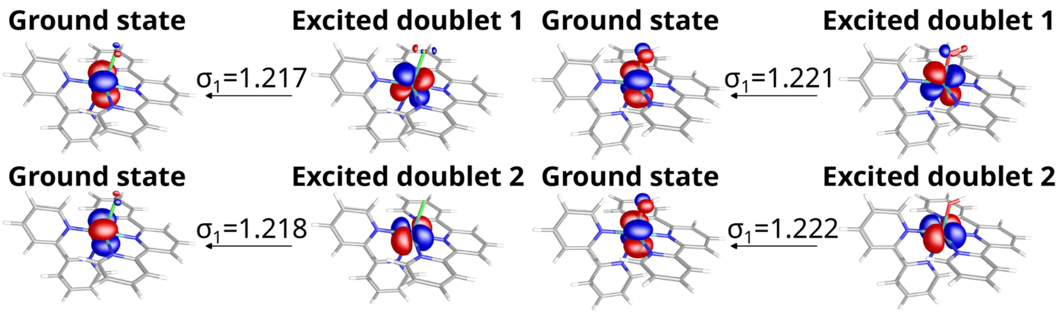

Fig. 5 Spinless triplet NTOs for $[\mathrm{Ru^{III}(bpy)(tpy)Cl}]^{2+}$ and $[\mathrm{Ru^{III}(bpy)(tpy)OH}]^{2+}$. The leading singular values are shown above the arrows.

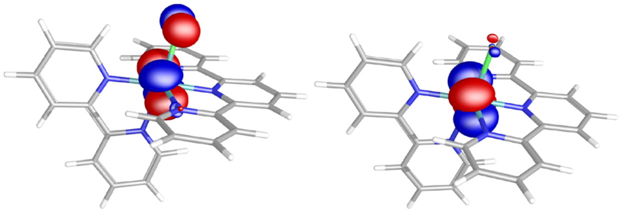

Fig. 6 Singly occupied spin-averaged natural orbital of the Kohn–Sham B3LYP determinant (left) and the SA-CASSCF for the lowest doublet state (right) for $[Ru^{III}(bpy)(tpy)Cl]^{2+}$.

experimental estimate of the Ru–OC bond length in $[Ru^{III}(N_4O)(H_2O)](ClO_4)_2$ of 1.961 Å and to the SA-CASSCF estimate of the Ru–OC bond length in *trans*-$[Ru^{III}(tpy)(Qc)H_2O]^{2+}$ of 1.911 Å (Table S2). The DFT and SA-CASSCF estimates of the Ru–OH_2 bond length in $[Ru^{III}(bpy)(tpy)H_2O]^{3+}$ disagree substantially. The active space does not include the orbitals describing the σ Ru–OH_2 bond; therefore, its CASSCF description may not include weak electron correlation affecting the length of this bond. The experimental estimate of the Ru–OH_2 bond length in $[Ru^{III}(N_4O)(H_2O)](ClO_4)_2$ is 2.115 Å,[134] which is in between the DFT and SA-CASSCF estimates in Table 2. The Ru–OH_2 bond length in *trans*-$[Ru^{III}(tpy)(Qc)H_2O]^{2+}$ found with SA-CASSCF is 2.214 Å (Fig. S2), which is close to the Ru–OH_2 bond length in $[Ru^{III}(bpy)(tpy)H_2O]^{3+}$ found in the same manner. Ethoxylation of the tpy ligands does not have a noticeable influence on the Ru–OH_2 bond length (Table S1).

The DFT and CASSCF estimates for the Ru–OH_2 bond length in *cis*- and *trans*-$[Ru^{III}(bpy)_2(H_2O)_2]^{3+}$ agree well. The experimental estimate of the Ru–O bond length in *trans*-$[Ru^{III}(bpy)_2(H_2O)(OH)](ClO_4)_2$ is 2.007 Å,[135] which is expected to be in between Ru–OH and Ru–OH_2 bond lengths due to its hydrogen-bonded crystal structure. Because of that, theoretical estimates also agree with this experimental estimate. Table 3 shows that the Ru–OH_2 bond lengths differ substantially between the isomers. The *cis* isomer has noticeably longer bonds, which is probably due to the repulsion between the lone pairs of H_2O.

The Ru–N bond lengths depend strongly on the nature of the ligands containing N. The Ru–N bond with the central N from tpy is rather short, ranging between 1.961 and 2.044 Å for all the compounds (SA-CASSCF). The Ru–N bond with the terminal N from tpy is longer, ranging between 2.116 and 2.158 Å (SA-CASSCF). The estimates obtained with B3LYP and SA-CASSCF for the Ru–N bonds with the tpy ligand agree well in all the cases. The likely reason behind the longer bonds with the terminal nitrogens is in the steric strain of the conjugated aromatic rings. Ethoxylation of the tpy shortens the Ru–N bond with the central nitrogen and elongates the bonds with the terminal nitrogens, which is likely due to the electron density redistribution in the aromatic rings influenced by the π-donating ethoxy tail. The Ru–N bonds with the bpy ligands are more variable, ranging between 2.063 and 2.154 Å (SA-CASSCF). These estimates are within the ranges of the experimentally determined Ru–N bond lengths for bpy ligands: 2.090 and 2.099 Å for *trans*-$[Ru^{III}(bpy)_2(H_2O)(OH)](ClO_4)_2$ from ref. 135; 2.050 and 2.060 Å for $[Ru^{III}(bpy)_2Cl_2]Cl$ from ref. 133. Disagreements in the Ru–N bond lengths between DFT and SA-CASSCF for bpy are larger than for tpy ligands, but the trends are preserved. The Ru–N bonds in *cis*- and *trans*-$[Ru^{III}(bpy)_2(H_2O)_2]^{3+}$ have different lengths. The *cis* isomer has shorter Ru–N bond lengths than the *trans* isomer. This is also consistent with the experimentally determined structure of *cis*-$[Ru^{III}(bpy)_2Cl_2]Cl$, which also has short Ru–N bonds.

Tables S2 and S3 show the bond lengths between Ru and ligands for *N*-oxide compounds. The Ru–O bond lengths are similar for all three compounds. The Ru–N bond lengths depend on the nature of ligands. The Ru–N bond lengths in $[Ru^{III}(bpy)_2(bpy\text{-}NO)]^{3+}$ are comparable with the Ru–N bond lengths for other complexes with bpy ligands. For dpp-NO and dpp-NO,NO ligands, the Ru–N bond lengths agree with each other and are close to the Ru–N bond lengths for tpy ligands. The Ru–N bond lengths for the central nitrogen atoms are short, while the Ru–N bond lengths of the terminal nitrogen atoms are long, consistent with the compounds with tpy ligands. For the pic ligand, the Ru–N bond lengths also agree with each other and are close to the Ru–N bond lengths for other complexes with pic ligands.

4.3 Calculations of the *g*-tensor

The fact that the three lowest doublet states are the main contributors to the *g*-tensors is not surprising because of the near degeneracy, the strong spin–orbit couplings (due to the local generalized the El-Sayed–Kanamori rules that we investigate in Section 4.1) and because of the large value of the transition angular momentum.

The estimates are sensitive to the energies used to evaluate the *g*-tensor components and change noticeably from CASSCF to NEVPT2 energies. Going to the full QD-NEVPT2 estimates introduces smaller changes in the resulting estimates. This is not surprising since the dynamic correlation has a rather modest influence on the strong spin–orbit couplings. The singular values in Fig. 5 are close to the maximum value possible for single-determinant wave-functions $\left(\sqrt{3/2}\right)$. The dynamic correlation can partly "wash away" the electron density from these NTO pairs, slightly reducing the resulting spin–orbit couplings and the *g*-tensor anisotropies, which is the case for most of the reported NEVPT2 and QD-NEVPT2 values.

In most cases, usage of the state averaging over only three doublet states leads to a better agreement with the experimental estimates, which is not surprising since only 3 lowest doublet states are the main contributors to the *g*-tensor anisotropy. This observation is consistent with the benchmarks from ref. 136, where averaging over a large number of electronic states also worsened agreement with experiments. The statistical behavior in Fig. 3, such as the coefficient of determination and the slope of linear regression, are very similar to the reported NEVPT2 benchmarks for complexes of 3d elements,[120] indicating that the trends are general across different elements. The authors of ref. 120 explain their observations through a lack of covalency of the NEVPT2 description

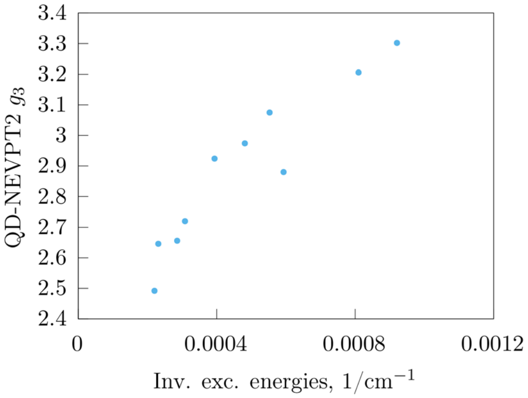

Fig. 7 The largest component of the *g*-tensor *vs.* inverse excitation energy.

that it inherits from CASSCF. While our reasoning is related to the lack of covalency, our explanation is different and relies on the difference between state density matrices of electronic states. Electronic screening impacts the degree of charge transfer, doing so differently for different electronic states. We observed similar trends in superexchange-modulated Néel temperatures in transition-metal oxides,[128] where treatment of electronic screening changed the slopes of the trends.

The calculated *g*-tensor values for all the considered compounds can be explained through the excitation energies. Since the g_3 component mostly depends only on the first excited state, we used it to track the dependence on the first excitation energy in Fig. 7, which shows the dependence of g_3 on the inverse excitation energy to the first doublet. The g_3 values are correlated well with the inverse excitation energies. Thus, the first excitation energy largely determines anisotropy of this component in these compounds.

The *g*-tensor values of the considered complexes have a different sensitivity to the used geometry. For $[\mathrm{Ru^{III}(bpy)(tpy)Cl}]^{2+}$, the estimates disagree more than by 0.2 for the *g*-tensor components evaluated at different geometries. For $[\mathrm{Ru^{III}(bpy)(tpy)OH}]^{2+}$, *cis*, *trans*-$[\mathrm{Ru^{III}(bpy)_2(H_2O)_2}]^{3+}$, the estimates are rather insensitive to the used geometries. The biggest disagreements in the *g*-tensor components for them is only 0.1. The reason behind this different behavior is likely due to the different excitation energies (Table 4). The excitation energy to the first excited doublet state in $[\mathrm{Ru^{III}(bpy)(tpy)Cl}]^{2+}$ is just 1809 cm^{-1} (QD-NEVPT2). Geometry perturbations can induce changes in excitation energies comparable with the vibrational levels. Therefore, the position of the doublet state can be affected; *g*-tensor estimates are affected too because of the large relative change in the position of the first excited doublet state. For $[\mathrm{Ru^{III}(bpy)(tpy)OH}]^{2+}$, *cis*, *trans*-$[\mathrm{Ru^{III}(bpy)_2(H_2O)_2}]^{3+}$, the first excitation energy is much higher. Hence, the relative changes in the excitation energies are smaller; therefore, the *g*-tensors estimates are less sensitive to the used geometry.

We tested the dependence of the *g*-tensor estimates on the presence of explicit water molecules. For $[\mathrm{Ru^{III}(bpy)(tpy)OH}]^{2+}$, the water molecules introduce almost no influence on the estimates, which is expected due to insensitivity to small perturbation of excitation energies. For $[\mathrm{Ru^{III}(bpy)(tpy)Cl}]^{2+}$, the water molecules change the *g*-tensor components by 0.1–0.2. This change is not surprising since the relative changes in the low excitation energy are noticeable even for small perturbations.

We observe the highest errors in *g*-tensor components for the cases with high anisotropy, which typically involve only a water ligand and organic ligands with donating nitrogen atoms. This is expected, since for such cases ligand orbitals do not mix substantially with the non-bonding orbitals on Ru. As a result, the non-bonding orbitals are nearly atomic and very close in energies. Therefore, the doublet electronic states are also close in energies. Due to a low excitation energy, the relative error in the *g*-tensor components is large. This observation is consistent with previous work.[54] This error can come from a variety of sources: an imperfect geometry (CASSCF does not include a sufficiently weak electron correlation to describe Ru bonds), solvation effects, and even vibronic effects, which can be substantial since the electronic excitation energies are comparable with the vibrational excitation energies. Nonetheless, the trends are reproduced. For example, ethoxylation of tpy increases the *g*-tensor anisotropy, which we now confirm theoretically. The *cis* isomer of $[\mathrm{Ru^{III}(bpy)_2(H_2O)_2}]^{3+}$ is more anisotropic than the *trans* isomer, which we also observe in calculations (however, interpretation of the experimental reference data requires caution because these compounds are acidic[137] and can lose H$^+$ if the pH is not low enough).

The errors of the *g*-tensor estimates for $[\mathrm{Ru^{III}(bpy)_2(bpy\text{-}NO)}]^{3+}$ are relatively large, which may be due to a potential influence of the aromatic system on the local charge on O. The estimates for the hypothetical $[\mathrm{Ru^{III}(pic)_2(dpp\text{-}NO)}]^{3+}$ intermediate have errors similar to $[\mathrm{Ru^{III}(bpy)_2(bpy\text{-}NO)}]^{3+}$. The errors for the hypothetical $[\mathrm{Ru^{III}(pic)_2(dpp\text{-}NO,NO)}]^{3+}$ intermediate are relatively small making this assignment plausible.

The first excitation energies in $[\mathrm{Ru^{III}(EtO\text{-}tpy)(pic)_2OH}]^{2+}$ and $[\mathrm{Ru^{III}(EtO\text{-}tpy)(pic)_2OOH}]^{2+}$ are close. Together with the similarity of the orbital shapes, these observations explain why the computed g_3 components are almost identical for these compounds. However, g_1 and g_2 are noticeably different, which one can use to distinguish these intermediates experimentally.

5 Conclusions

We presented detailed electronic structure benchmarks for Ru$^{\mathrm{III}}$ complexes. We showed that in all the considered species, the three nearly degenerate doublet states are responsible for *g*-tensor anisotropies of these species. We showed that the origin of these doublets lies in the distribution of a hole over 3 non-bonding 4d orbitals on Ru, which we investigated using spin-averaged natural orbitals and spinless triplet natural transition orbitals. A partial mixing of the orbitals from ligands increases the energy difference between the electronic states. We viewed the role of dynamic correlation through the electronic screening and rationalized it from the partial weights of the ligand orbitals in the singly occupied natural orbitals.

Based on the insights from the electronic structure, we constructed a computational protocol that allowed us to investigate the influence of different factors on the *g*-tensor estimates. We found that the errors in the SA-CASSCF geometries for Ru^{III} species are comparable with the previously reported errors for Ru^{II} complexes.[132] We also attributed some of the possible errors in DFT geometries through charge delocalization errors.

We computed *g*-tensors for a variety of species and showed that using state averaging over only 3 nearly degenerate doublets produces better estimates. This is not surprising since these 3 doublets are the most important states determining the *g*-tensor. We showed that depending on the excitation energies, the *g*-tensors have different sensitivities to factors, such as geometries and solvation. The lower the excitation energy is, the bigger its relative change is with respect to such a perturbation. As a result, the changes in the *g*-tensor components also become large for the species with low excitation energies. Species with high excitation energies are insensitive to such perturbations. For these species, theoretical estimates of the *g*-tensors can even reach the experimental accuracy. We apply the analysis and the observed trends and provide computational evidence toward the previous assignment of the hypothetical intermediates $[Ru^{III}(pic)_2(dpp\text{-}NO)]^{3+}$ and $[Ru^{III}(pic)_2(dpp\text{-}NO,NO)]^{3+}$. Finally, we provide theoretical insight that allows one to distinguish $[Ru^{III}(EtO\text{-}tpy)(pic)_2OH]^{2+}$ and $[Ru^{III}(EtO\text{-}tpy)(pic)_2OOH]^{2+}$ experimentally.

Conflicts of interest

The authors have no conflicts to disclose.

Data availability

The data supporting this article have been included as part of the supplementary information (SI) and the uploaded geoms.zip archive. Supplementary information: experimental EPR spectrum, additional tables with bond lengths and *g*-tensors, and plots with natural orbitals. The geometries are available in xyz format in a separate archive. See DOI: **https://doi.org/10.1039/d5cp03298a**.

Acknowledgements

NSF, CHE-2155060 (Y. P.) supported this research. Access to EPR was provided by the Amy Instrumentation Facility, Department of Chemistry, under the supervision of Dr Michael Everly. The EPR spectrum of the $[Ru^{III}(tpy)(bpy)(OH)]^{2+}$ was recorded by Dr Guibo Zho. We thank Prof. Anna Krylov for carefully reading the manuscript and providing feedback.

Notes and references

1 M. Goswami, A. Chirila, C. Rebreyend and B. de Bruin, EPR Spectroscopy as a Tool in Homogeneous Catalysis Research, *Top. Catal.*, 2015, **58**, 719–750.

2 S. A. Bonke, T. Risse, A. Schnegg and A. Brückner, In situ electron paramagnetic resonance spectroscopy for catalysis, *Nat. Rev. Methods Primers*, 2021, **1**, 33.

3 M. Hunger and J. Weitkamp, In situ IR, NMR, EPR, and UV/Vis Spectroscopy: Tools for New Insight into the Mechanisms of Heterogeneous Catalysis, *Angew. Chem., Int. Ed.*, 2001, **40**, 2954–2971.

4 M. Chiesa, E. Giamello and M. Che, EPR Characterization and Reactivity of Surface-Localized Inorganic Radicals and Radical Ions, *Chem. Rev.*, 2010, **110**, 1320–1347.

5 A. Hoff, *Advanced EPR: Applications in Biology and Biochemistry*, Elsevier Science, 1989.

6 T. Prisner, M. Rohrer and F. MacMillan, Pulsed EPR Spectroscopy: Biological Applications, *Annu. Rev. Phys. Chem.*, 2001, **52**, 279–313.

7 C. Balakrishnan and M. A. Neelakantan, Crystal structure and bio-catalytic potential of oxovanadium(IV) Schiff base complexes derived from 2-hydroxy-4-(prop-2-yn-1-yloxy)benzaldehyde and alicyclic/aromatic diamines, *Inorg. Chim. Acta*, 2018, **469**, 503–514.

8 D. P. Goldberg, J. Telser, J. Krzystek, A. G. Montalban, L.-C. Brunel, A. G. M. Barrett and B. M. Hoffman, EPR Spectra from "EPR-Silent" Species: High-Field EPR Spectroscopy of Manganese(III) Porphyrins, *J. Am. Chem. Soc.*, 1997, **119**, 8722–8723.

9 K. A. Campbell, M. R. Lashley, J. K. Wyatt, M. H. Nantz and R. D. Britt, Dual-Mode EPR Study of Mn(III) Salen and the Mn(III) Salen-Catalyzed Epoxidation of *cis*-β-Methylstyrene, *J. Am. Chem. Soc.*, 2001, **123**, 5710–5719.

10 O. Y. Lyakin, K. P. Bryliakov and E. P. Talsi, EPR, 1H and 2H NMR, and Reactivity Studies of the Iron–Oxygen Intermediates in Bioinspired Catalyst Systems, *Inorg. Chem.*, 2011, **50**, 5526–5538.

11 K. C. Christoforidis, M. Louloudi, E. R. Milaeva, Y. Sanakis and Y. Deligiannakis, EPR study of a novel [Fe-porphyrin] catalyst, *Mol. Phys.*, 2007, **105**, 2185–2194.

12 O. Y. Lyakin, A. M. Zima, D. G. Samsonenko, K. P. Bryliakov and E. P. Talsi, EPR Spectroscopic Detection of the Elusive $Fe^{V} = O$ Intermediates in Selective Catalytic Oxofunctionalizations of Hydrocarbons Mediated by Biomimetic Ferric Complexes, *ACS Catal.*, 2015, **5**, 2702–2707.

13 G. E. Cutsail III, B. W. Stein, D. Subedi, J. M. Smith, M. L. Kirk and B. M. Hoffman, EPR, ENDOR, and Electronic Structure Studies of the Jahn-Teller Distortion in an Fe^{V} Nitride, *J. Am. Chem. Soc.*, 2014, **136**, 12323–12336.

14 V. Saraev and F. Shmidt, EPR for catalysts based on nickel and cobalt complexes, *J. Mol. Catal. A: Chem.*, 2000, **158**, 149–154.

15 W. I. Dzik, X. Xu, X. P. Zhang, J. N. H. Reek and B. de Bruin, 'Carbene Radicals' in Co^{II} (por)-Catalyzed Olefin Cyclopropanation, *J. Am. Chem. Soc.*, 2010, **132**, 10891–10902.

16 W. J. M. Blackaby, S. Sabater, R. C. Poulten, M. J. Page, A. Folli, V. Krewald, M. F. Mahon, D. M. Murphy, E. Richards and M. K. Whittlesey, Mono- and dinuclear Ni(I) products formed upon bromide abstraction from

the Ni(I) ring-expanded NHC complex [Ni(6-Mes)(PPh3)Br], *Dalton Trans.*, 2018, **47**, 769–782.

17 D. Zois, C. Vartzouma, Y. Deligiannakis, N. Hadjiliadis, L. Casella, E. Monzani and M. Louloudi, Active catalytic centers in silica-supported Cu(II) and Mn(II) biomimetic complexes: Correlation between catalytic and EPR data, *J. Mol. Catal. A: Chem.*, 2007, **261**, 306–317.

18 V. N. Nemykin, J. R. Sabin, B. W. Kail, A. Upadhyay, M. P. Hendrich and P. Basu, Influence of the ligand-field on EPR parameters of *cis*- and *trans*-isomers in Mo^V systems relevant to molybdenum enzymes: Experimental and density functional theory study, *J. Inorg. Biochem.*, 2023, **245**, 112228.

19 A. Rajapakshe, R. A. Snyder, A. V. Astashkin, P. Bernardson, D. J. Evans, C. G. Young, D. H. Evans and J. H. Enemark, Insights into the nature of Mo(V) species in solution: Modeling catalytic cycles for molybdenum enzymes, *Inorg. Chim. Acta*, 2009, **362**, 4603–4608.

20 P. A. Poltarak, V. Y. Komarov, S. G. Kozlova, V. A. Nadolinnyi, A. A. Poltarak, S. B. Artemkina and V. E. Fedorov, New Molecular Niobium(IV) Complexes NbX4(OPPh3)2 (X = Cl, Br): Synthesis, Crystal and Electronic Structure, *J. Struct. Chem.*, 2019, **60**, 457–465.

21 E. W. Y. Wong, C. J. Walsby, T. Storr and D. B. Leznoff, Phthalocyanine as a Chemically Inert, Redox-Active Ligand: Structural and Electronic Properties of a Nb(IV)-Oxo Complex Incorporating a Highly Reduced Phthalocyanine(4-) Anion, *Inorg. Chem.*, 2010, **49**, 3343–3350.

22 F. F. Puschmann, J. Harmer, D. Stein, H. Rüegger, B. de Bruin and H. Grützmacher, Electromeric Rhodium Radical Complexes, *Angew. Chem., Int. Ed.*, 2010, **49**, 385–389.

23 D. Menglet, A. M. Bond, K. Coutinho, R. S. Dickson, G. G. Lazarev, S. A. Olsen and J. R. Pilbrow, EPR, Electronic Spectra, and Electron Transfer Properties of the 17 Electron Carbonylhydrotris(triphenylphosphine)rhodium(II) Cation, *J. Am. Chem. Soc.*, 1998, **120**, 2086–2089.

24 B. B. Wayland, A. E. Sherry and A. G. Bunn, EPR studies of 1 : 1 complexes of rhodium(II) and cobalt(II) porphyrins with σ donor and π acceptor ligands: origins of rhodium(II) metalloradical reactivity, *J. Am. Chem. Soc.*, 1993, **115**, 7675–7684.

25 D. Moonshiram, I. Alperovich, J. J. Concepcion, T. J. Meyer and Y. Pushkar, Experimental demonstration of radicaloid character in a $Ru^V = O$ intermediate in catalytic water oxidation, *Proc. Natl. Acad. Sci. U. S. A.*, 2013, **110**, 3765–3770.

26 S. Bernhard, J. A. Barron, P. L. Houston, H. D. Abruña, J. L. Ruglovksy, X. Gao and G. G. Malliaras, Electroluminescence in Ruthenium(II) Complexes, *J. Am. Chem. Soc.*, 2002, **124**, 13624–13628.

27 S. Y. Lee, C. Y. Kim and T.-G. Nam, Ruthenium Complexes as Anticancer Agents: A Brief History and Perspectives, *Drug Des., Dev. Ther.*, 2020, **14**, 5375–5392.

28 T. P. Montgomery, A. M. Johns and R. H. Grubbs, Recent Advancements in Stereoselective Olefin Metathesis Using Ruthenium Catalysts, *Catalysts*, 2017, **7**, 87.

29 M. Albrecht and G. van Koten, Platinum Group Organometallics Based on ''Pincer'' Complexes: Sensors, Switches, and Catalysts, *Angew. Chem., Int. Ed.*, 2001, **40**, 3750–3781.

30 Y. Izumi and K. Aika, Promoted Catalysis by Supported [Ru6N] Clusters in N2 and/or H2: Structural and Chemical Controls, *J. Phys. Chem.*, 1995, **99**, 10346–10353.

31 V. S. Thirunavukkarasu, S. I. Kozhushkov and L. Ackermann, C–H nitrogenation and oxygenation by ruthenium catalysis, *Chem. Commun.*, 2014, **50**, 29–39.

32 F. Kakiuchi, T. Kochi, E. Mizushima and S. Murai, Room-Temperature Regioselective C-H/Olefin Coupling of Aromatic Ketones Using an Activated Ruthenium Catalyst with a Carbonyl Ligand and Structural Elucidation of Key Intermediates, *J. Am. Chem. Soc.*, 2010, **132**, 17741–17750.

33 S. W. Gersten, G. J. Samuels and T. J. Meyer, Catalytic oxidation of water by an oxo-bridged ruthenium dimer, *J. Am. Chem. Soc.*, 1982, **104**, 4029–4030.

34 J. M. Kamdar and D. B. Grotjahn, An Overview of Significant Achievements in Ruthenium-Based Molecular Water Oxidation Catalysis, *Molecules*, 2019, **24**, 494.

35 L. Tong and R. P. Thummel, Mononuclear ruthenium polypyridine complexes that catalyze water oxidation, *Chem. Sci.*, 2016, **7**, 6591–6603.

36 R. Matheu, P. Garrido-Barros, M. Gil-Sepulcre, M. Z. Ertem, X. Sala, C. Gimbert-Suriñach and A. Llobet, The development of molecular water oxidation catalysts, *Nat. Rev. Chem.*, 2019, **3**, 331–341.

37 D. W. Shaffer, Y. Xie and J. J. Concepcion, O–O bond formation in ruthenium-catalyzed water oxidation: single-site nucleophilic attack *vs.* O–O radical coupling, *Chem. Soc. Rev.*, 2017, **46**, 6170–6193.

38 D. Moonshiram, Y. Pineda-Galvan, D. Erdman, M. Palenik, R. Zong, R. Thummel and Y. Pushkar, Uncovering the Role of Oxygen Atom Transfer in Ru-Based Catalytic Water Oxidation, *J. Am. Chem. Soc.*, 2016, **138**, 15605–15616.

39 Y. Pineda-Galvan, A. K. Ravari, S. Shmakov, L. Lifshits, N. Kaveevivitchai, R. Thummel and Y. Pushkar, Detection of the site protected 7-coordinate Ru(V) = O species and its chemical reactivity to enable catalytic water oxidation, *J. Catal.*, 2019, **375**, 1–7.

40 A. K. Ravari, G. Zhu, R. Ezhov, Y. Pineda-Galvan, A. Page, W. Weinschenk, L. Yan and Y. Pushkar, Unraveling the Mechanism of Catalytic Water Oxidation *via* de Novo Synthesis of Reactive Intermediate, *J. Am. Chem. Soc.*, 2020, **142**, 884–893.

41 Y. Pushkar, D. Moonshiram, V. Purohit, L. Yan and I. Alperovich, Spectroscopic Analysis of Catalytic Water Oxidation by $[Ru^{II}(bpy)(tpy)H_2O]^{2+}$ Suggests That $Ru^V = O$ Is Not a Rate-Limiting Intermediate, *J. Am. Chem. Soc.*, 2014, **136**, 11938–11945.

42 N. Planas, L. Vigara, C. Cady, P. Miró, P. Huang, L. Hammarström, S. Styring, N. Leidel, H. Dau, M. Haumann, L. Gagliardi, C. J. Cramer and A. Llobet, Electronic Structure of Oxidized Complexes Derived from *cis*-$[Ru^{II}(bpy)_2(H_2O)_2]^{2+}$ and Its Photoisomerization Mechanism, *Inorg. Chem.*, 2011, **50**, 11134–11142.

43 A. K. Ravari, Y. Pineda-Galvan, A. Huynh, R. Ezhov and Y. Pushkar, Facile Light-Induced Transformation of $[Ru^{II}(bpy)_2(bpyNO)]^{2+}$ to $[Ru^{II}(bpy)_3]^{2+}$, *Inorg. Chem.*, 2020, **59**, 13880–13887.

44 J. Patel, G. Bury, A. K. Ravari, R. Ezhov and Y. Pushkar, Systematic Influence of Electronic Modification of Ligands on the Catalytic Rate of Water Oxidation by a Single-Site Ru-Based Catalyst, *ChemSusChem*, 2022, **15**, e202101657.

45 These are hypothetical intermediates, for which the experimental support is scarce. While several claims of possible detection of the peroxo species in Ru based WOC have been noted,[38,44,138,139] none were firmly confirmed by either the correct isotope pattern, non-congested vibrational spectra or by 2nd independent detection method. Interestingly, in the past Ru complex with *N*-oxide modified ligand was misinterpreted to be assigned to peroxo species.[138] So, we are currently not aware of any reported and firmly assigned Ru^{III} complex with –OOH ligand. Thus, predicting *g*-tensor of such species might be beneficial to evaluate if EPR can be used for confirming such peroxide in combination with vibrational methods.

46 J. Patel, G. Bury and Y. Pushkar, Rational Design of Improved Ru Containing Fe-Based Metal-Organic Framework (MOF) Photoanode for Artificial Photosynthesis, *Small*, 2024, **20**, 2310106.

47 This is a hypothetical but plausable assignment because of insufficient experimental evidence. Oxidative reactions with Ru complexes can go through a number of pathways, including oxidation of lidangs, which form the hypothetical *N*-oxides. In the current work, we provide additional computational evidence confirming this assignment.

48 X. Yang and M.-H. Baik, *cis*,*cis*-$[(bpy)_2Ru^VO]_2O^{4+}$ Catalyzes Water Oxidation Formally via in Situ Generation of Radicaloid Ru^{IV}-O, *J. Am. Chem. Soc.*, 2006, **128**, 7476–7485.

49 X. Yang and M.-H. Baik, Electronic Structure of the Water-Oxidation Catalyst $[(bpy)_2(OH_x)RuORu(OH_y)(bpy)_2]^{z+}$: Weak Coupling between the Metal Centers Is Preferred over Strong Coupling, *J. Am. Chem. Soc.*, 2004, **126**, 13222–13223.

50 S. Ghosh and M.-H. Baik, Redox Properties of Tanaka's Water Oxidation Catalyst: Redox Noninnocent Ligands Dominate the Electronic Structure and Reactivity, *Inorg. Chem.*, 2011, **50**, 5946–5957.

51 X. Sala, M. Z. Ertem, L. Vigara, T. K. Todorova, W. Chen, R. C. Rocha, F. Aquilante, C. J. Cramer, L. Gagliardi and A. Llobet, The *cis*-$[Ru^{II}(bpy)_2(H_2O)_2]^{2+}$ Water-Oxidation Catalyst Revisited, *Angew. Chem., Int. Ed.*, 2010, **49**, 7745–7747.

52 L. Vigara, M. Z. Ertem, N. Planas, F. Bozoglian, N. Leidel, H. Dau, M. Haumann, L. Gagliardi, C. J. Cramer and A. Llobet, Experimental and quantum chemical characterization of the water oxidation cycle catalysed by $[Ru^{II}(damp)(bpy)(H_2O)]^{2+}$, *Chem. Sci.*, 2012, **3**, 2576–2586.

53 G. Bury and Y. Pushkar, Computational Analysis of Structure-Activity Relationships in Highly Active Homogeneous Ruthenium-Based Water Oxidation Catalysts, *Catalysts*, 2022, **12**, 863.

54 H. Bolvin, Theoretical Determination of the Excited States and of g-Factors of the Creutz-Taube Ion, $[(NH_3)_5$-Ru-pyrazine-Ru-$(NH_3)_5]^{5+}$, *Inorg. Chem.*, 2007, **46**, 417–427.

55 L. Dubicki and E. Krausz, Electronic coupling in trigonal mixed-valence dimers and the MCD and EPR spectra of tris(.mu.-halo)bis(triammineruthenium)(2+) ions, *Inorg. Chem.*, 1985, **24**, 4461–4465.

56 L. Dubicki, J. Ferguson and E. R. Krausz, Electronic coupling in delocalized mixed-valence dimers, *J. Am. Chem. Soc.*, 1985, **107**, 179–182.

57 L. F. Chibotaru, A. Ceulemans and H. Bolvin, Unique Definition of the Zeeman-Splitting *g* Tensor of a Kramers Doublet, *Phys. Rev. Lett.*, 2008, **101**, 033003.

58 M. Kaupp, in *Ab Initio and Density Functional Calculations of Electronic g-Tensors for Organic Radicals*, ed. A. Lund and M. Shiotani, Springer, Netherlands, Dordrecht, 2013, pp. 323–361.

59 J. Autschbach, in *Relativistic Effects on Magnetic Resonance Parameters and Other Properties of Inorganic Molecules and Metal Complexes*, ed. M. Barysz and Y. Ishikawa, Springer, Netherlands, Dordrecht, 2010, pp. 521–598.

60 F. Neese, *Quantum Chemistry and EPR Parameters*, John Wiley & Sons, Ltd, 2017, pp. 1–22.

61 H. Bolvin and J. Autschbach, in *Relativistic Methods for Calculating Electron Paramagnetic Resonance (EPR) Parameters*, ed. W. Liu, Springer Berlin Heidelberg, Berlin, Heidelberg, 2014, pp. 1–39.

62 P.-Å. Malmqvist, B. O. Roos and B. Schimmelpfennig, The restricted active space (RAS) state interaction approach with spin–orbit coupling, *Chem. Phys. Lett.*, 2002, **357**, 230–240.

63 H. Bolvin, An Alternative Approach to the g-Matrix: Theory and Applications, *ChemPhysChem*, 2006, **7**, 1575–1589.

64 S. Vancoillie, P.-A. Malmqvist and K. Pierloot, Calculation of EPR g Tensors for Transition-Metal Complexes Based on Multiconfigurational Perturbation Theory (CASPT2), *ChemPhysChem*, 2007, **8**, 1803–1815.

65 C. Zhou, D. Wu, L. Gagliardi and D. G. Truhlar, Calculation of the Zeeman Effect for Transition-Metal Complexes by Multiconfiguration Pair-Density Functional Theory, *J. Chem. Theory Comput.*, 2021, **17**, 5050–5063.

66 P. Pokhilko, E. Epifanovsky and A. I. Krylov, General framework for calculating spin-orbit couplings using spinless one-particle density matrices: theory and application to the equation-of-motion coupled-cluster wave functions, *J. Chem. Phys.*, 2019, **151**, 034106.

67 A. Carreras, H. Jiang, P. Pokhilko, A. Krylov, P. M. Zimmerman and D. Casanova, Calculation Of Spin-orbit Couplings Using RASCI Spinless One-particle Density Matrices: Theory And Applications, *J. Chem. Phys.*, 2020, **153**, 214107.

68 S. Kähler, A. Cebreiro, P. Pokhilko, D. Casanova and A. I. Krylov, State-interaction approach for evaluating g-tensors within EOM-CC and RAS-CI frameworks: Theory and benchmarks, *J. Phys. Chem. A*, 2023, **127**, 8459–8472.

69 E. R. Sayfutyarova and G. K.-L. Chan, A state interaction spin-orbit coupling density matrix renormalization group method, *J. Chem. Phys.*, 2016, **144**, 234301.

70 A. Cebreiro-Gallardo and D. Casanova, State-Interaction Approach for g-Matrix Calculations in TDDFT: Ground-Excited State Couplings and beyond First-Order Spin–Orbit Effects, *J. Chem. Theory Comput.*, 2025, **21**, 6528–6544.

71 M. Roemelt, Spin orbit coupling for molecular ab initio density matrix renormalization group calculations: Application to g-tensors, *J. Chem. Phys.*, 2015, **143**, 044112.

72 L. Lang and F. Neese, Spin-dependent properties in the framework of the dynamic correlation dressed complete active space method, *J. Chem. Phys.*, 2019, **150**, 104104.

73 T. N. Lan, J. Chalupský and T. Yanai, Molecular g-tensors from analytical response theory and quasi-degenerate perturbation theory in the framework of complete active space self-consistent field method, *Mol. Phys.*, 2015, **113**, 1750–1767.

74 O. Vahtras, B. Minaev and H. Ågren, Ab initio calculations of electronic g-factors by means of multiconfiguration response theory, *Chem. Phys. Lett.*, 1997, **281**, 186–192.

75 O. L. Malkina, J. Vaara, B. Schimmelpfennig, M. Munzarová, V. G. Malkin and M. Kaupp, Density Functional Calculations of Electronic g-Tensors Using Spin-Orbit Pseudopotentials and Mean-Field All-Electron Spin-Orbit Operators, *J. Am. Chem. Soc.*, 2000, **122**, 9206–9218.

76 F. Neese, Analytic derivative calculation of electronic g-tensors based on multireference configuration interaction wavefunctions, *Mol. Phys.*, 2007, **105**, 2507–2514.

77 J. Gauss, M. Kállay and F. Neese, Calculation of Electronic g-Tensors using Coupled Cluster Theory, *J. Phys. Chem. A*, 2009, **113**, 11541–11549.

78 P. Verma and J. Autschbach, Variational versus Perturbational Treatment of Spin-Orbit Coupling in Relativistic Density Functional Calculations of Electronic g Factors: Effects from Spin-Polarization and Exact Exchange, *J. Chem. Theory Comput.*, 2013, **9**, 1052–1067.

79 D. Ganyushin and F. Neese, A fully variational spin-orbit coupled complete active space self-consistent field approach: Application to electron paramagnetic resonance g-tensors, *J. Chem. Phys.*, 2013, **138**, 104113.

80 D. Jayatilaka, Electron spin resonance g tensors from general Hartree–Fock calculations, *J. Chem. Phys.*, 1998, **108**, 7587–7594.

81 S. G. Tabrizi, R. Rodríguez-Guzmán and C. A. Jiménez-Hoyos, Calculation of molecular g-tensors by sampling spin orientations of generalised Hartree-Fock states, *Mol. Phys.*, 2023, **121**, e2192820.

82 Y. Guo, K. Sivalingam and F. Neese, Approximations of density matrices in N-electron valence state second-order perturbation theory (NEVPT2). I. Revisiting the NEVPT2 construction, *J. Chem. Phys.*, 2021, **154**, 214111.

83 C. Angeli, S. Borini, M. Cestari and R. Cimiraglia, A quasidegenerate formulation of the second order n-electron valence state perturbation theory approach, *J. Chem. Phys.*, 2004, **121**, 4043–4049.

84 L. Lang, K. Sivalingam and F. Neese, The combination of multipartitioning of the Hamiltonian with canonical Van Vleck perturbation theory leads to a Hermitian variant of quasidegenerate N-electron valence perturbation theory, *J. Chem. Phys.*, 2020, **152**, 014109.

85 J. F. Stanton and J. Gauss, Analytic energy derivatives for ionized states described by the equation-of-motion coupled cluster method, *J. Chem. Phys.*, 1994, **101**, 8938–8944.

86 E. R. Sayfutyarova, Q. Sun, G. K.-L. Chan and G. Knizia, Automated Construction of Molecular Active Spaces from Atomic Valence Orbitals, *J. Chem. Theory Comput.*, 2017, **13**, 4063–4078.

87 C. Kollmar, K. Sivalingam, B. Helmich-Paris, C. Angeli and F. Neese, A perturbation-based super-CI approach for the orbital optimization of a CASSCF wave function, *J. Comput. Chem.*, 2019, **40**, 1463–1470.

88 F. Neese, Software update: the ORCA program system, version 5.0, *Wiley Interdiscip. Rev.:Comput. Mol. Sci.*, 2022, **12**, e1606.

89 Q. Sun, *Co-iterative augmented Hessian method for orbital optimization, arXiv*, 2017, preprint, arXiv:1610.08423, DOI: **10.48550/arXiv.1610.08423**, **https://arxiv.org/abs/1610.08423**.

90 Q. Sun, J. Yang and G. K.-L. Chan, A general second order complete active space self-consistent-field solver for large-scale systems, *Chem. Phys. Lett.*, 2017, **683**, 291–299.

91 Q. Sun, T. C. Berkelbach, N. S. Blunt, G. H. Booth, S. Guo, Z. Li, J. Liu, J. D. McClain, E. R. Sayfutyarova, S. Sharma, S. Wouters and G. K. Chan, PySCF: the Python-based simulations of chemistry framework, *Wiley Interdiscip. Rev.: Comput. Mol. Sci.*, 2017, **8**, e1340.

92 We used the PySCF version with git hash *142756584ed3963728cc1f6823286f4605811a6c* with local modifications as described in the text.

93 N. Godbout, D. R. Salahub, J. Andzelm and E. Wimmer, Optimization of Gaussian-type basis sets for local spin density functional calculations. Part I. Boron through neon, optimization technique and validation, *Can. J. Chem.*, 1992, **70**, 560–571.

94 P. C. Hariharan and J. A. Pople, *Theor. Chim. Acta*, 1973, **28**, 213.

95 M. M. Francl, W. J. Pietro, W. J. Hehre, J. S. Binkley, M. S. Gordon, D. J. DeFrees and J. A. Pople, Self-consistent molecular orbital methods. XXIII. A polarization-type basis set for second-row elements, *J. Chem. Phys.*, 1982, **77**, 3654–3665.

96 M. J. Frisch, G. W. Trucks, H. B. Schlegel, G. E. Scuseria, M. A. Robb, J. R. Cheeseman, G. Scalmani, V. Barone, B. Mennucci, G. A. Petersson, H. Nakatsuji, M. Caricato, X. Li, H. P. Hratchian, A. F. Izmaylov, J. Bloino, G. Zheng, J. L. Sonnenberg, M. Hada, M. Ehara, K. Toyota, R. Fukuda, J. Hasegawa, M. Ishida, T. Nakajima, Y. Honda, O. Kitao, H. Nakai, T. Vreven, J. A. Montgomery, Jr., J. E. Peralta, F. Ogliaro, M. Bearpark, J. J. Heyd, E. Brothers, K. N. Kudin, V. N. Staroverov, R. Kobayashi, J. Normand, K. Raghavachari, A. Rendell, J. C. Burant, S. S. Iyengar, J. Tomasi, M. Cossi, N. Rega, J. M. Millam, M. Klene, J. E. Knox, J. B. Cross, V. Bakken, C. Adamo, J. Jaramillo, R. Gomperts, R. E. Stratmann, O. Yazyev, A. J. Austin, R. Cammi, C. Pomelli, J. W. Ochterski, R. L. Martin,

K. Morokuma, V. G. Zakrzewski, G. A. Voth, P. Salvador, J. J. Dannenberg, S. Dapprich, A. D. Daniels, Ö. Farkas, J. B. Foresman, J. V. Ortiz, J. Cioslowski and D. J. Fox, *Gaussian09 Revision A.02*, Gaussian Inc., Wallingford CT, 2009.

97 J. Hermann, PYBERNY: Molecular structure optimizer. For the current version, see **https://github.com/jhrmnn/pyberny**.

98 J. Stålring, A. Bernhardsson and R. Lindh, Analytical gradients of a state average MCSCF state and a state average diagnostic, *Mol. Phys.*, 2001, **99**, 103–114.

99 T. H. Dunning, Jr., Gaussian basis sets for use in correlated molecular calculations. I. The atoms boron through neon and hydrogen, *J. Chem. Phys.*, 1989, **90**, 1007–1023.

100 D. E. Woon and T. H. Dunning, Gaussian basis sets for use in correlated molecular calculations. III. The atoms aluminum through argon, *J. Chem. Phys.*, 1993, **98**, 1358–1371.

101 F. Weigend and R. Ahlrichs, Balanced basis sets of split valence, triple zeta valence and quadruple zeta valence quality for H to Rn: Design and assessment of accuracy, *Phys. Chem. Chem. Phys.*, 2005, **7**, 3297.

102 D. Andrae, U. Häußermann, M. Dolg, H. Stoll and H. Preuß, Energy-adjusted ab initio pseudopotentials for the second and third row transition elements, *Theor. Chim. Acta*, 1990, **77**, 123–141.

103 F. Weigend, A fully direct RI-HF algorithm: Implementation, optimised auxiliary basis sets, demonstration of accuracy and efficiency, *Phys. Chem. Chem. Phys.*, 2002, **4**, 4285–4291.

104 A. Hellweg, C. Hättig, S. Höfener and W. Klopper, Optimized accurate auxiliary basis sets for RI-MP2 and RI-CC2 calculations for the atoms Rb to Rn, *Theor. Chim. Acta*, 2007, **117**, 587–597.

105 A. H. Baker, *On improving the performance of the linear solver restarted GMRES*, University of Colorado at Boulder, 2003.

106 A. H. Baker, E. R. Jessup and T. Manteuffel, A Technique for Accelerating the Convergence of Restarted GMRES, *SIAM J. Matrix Anal. Appl.*, 2005, **26**, 962–984.

107 J. W. Furness, A. D. Kaplan, J. Ning, J. P. Perdew and J. Sun, Accurate and Numerically Efficient r^{2}SCAN Meta-Generalized Gradient Approximation, *J. Phys. Chem. Lett.*, 2020, **11**, 8208–8215.

108 W. Kutzelnigg and W. Liu, Quasirelativistic theory equivalent to fully relativistic theory, *J. Chem. Phys.*, 2005, **123**, 241102.

109 D. Peng, N. Middendorf, F. Weigend and M. Reiher, An efficient implementation of two-component relativistic exact-decoupling methods for large molecules, *J. Chem. Phys.*, 2013, **138**, 184105.

110 B. O. Roos, R. Lindh, P.-A. Malmqvist, V. Veryazov and P.-O. Widmark, New Relativistic ANO Basis Sets for Transition Metal Atoms, *J. Phys. Chem. A*, 2005, **109**, 6575–6579.

111 G. L. Stoychev, A. A. Auer and F. Neese, Automatic Generation of Auxiliary Basis Sets, *J. Chem. Theory Comput.*, 2017, **13**, 554–562.

112 D. Ganyushin and F. Neese, First-principles calculations of zero-field splitting parameters, *J. Chem. Phys.*, 2006, **125**, 024103.

113 F. Neese, Efficient and accurate approximations to the molecular spin-orbit coupling operator and their use in molecular g-tensor calculations, *J. Chem. Phys.*, 2005, **122**, 034107.

114 P. Pokhilko and A. I. Krylov, Quantitative El-Sayed Rules for Many-Body Wavefunctions from Spinless Transition Density Matrices, *J. Phys. Chem. Lett.*, 2019, **10**, 4857–4862.

115 A. Allouche, Gabedit-a graphical user interface for computational chemistry softwares, *J. Comput. Chem.*, 2011, **32**, 174–182.

116 Persistence of Vision (TM) Raytracer.

117 M. Lundber and P. Siegbahn, Quantifying the effects of the self-interaction error in DFT: When do the delocalized states appear?, *J. Chem. Phys.*, 2005, **122**, 224103.

118 B. G. Johnson, C. A. Gonzales, P. M. Gill and J. A. Pople, A density functional study of the simplest hydrogen abstraction reaction. Effect of self-interaction correction, *Chem. Phys. Lett.*, 1994, **221**, 100–108.

119 B. Rana and J. M. Herbert, Hidden Hemibonding in the Aqueous Hydroxyl Radical, *J. Phys. Chem. Lett.*, 2021, **12**, 8053–8060.

120 S. K. Singh, M. Atanasov and F. Neese, Challenges in Multireference Perturbation Theory for the Calculations of the g-Tensor of First-Row Transition-Metal Complexes, *J. Chem. Theory Comput.*, 2018, **14**, 4662–4677.

121 T. Soda, Y. Kitagawa, T. Onishi, Y. Takano, Y. Shigeta, H. Nagao, Y. Yoshioka and K. Yamaguchi, Ab initio computations of effective exchange integrals for H-H, H-He-H and Mn_2O_2 complex: comparison of broken-symmetry approaches, *Chem. Phys. Lett.*, 2000, **319**, 223–230.

122 P. Pokhilko and D. Zgid, Interpretation of multiple solutions in fully iterative GF2 and GW schemes using local analysis of two-particle density matrices, *J. Chem. Phys.*, 2021, **155**, 024101.

123 P. Pokhilko, C.-N. Yeh, M. A. Morales and D. Zgid, Tensor hypercontraction for self-consistent vertex corrected GW with static and dynamic screening; applications to molecules and solids with superexchange, *J. Chem. Phys.*, 2025, **162**, 244110.

124 P. Pokhilko and D. Zgid, Natural orbitals and two-particle correlators as tools for the analysis of effective exchange couplings in solids, *Phys. Chem. Chem. Phys.*, 2023, **25**, 21267–21279.

125 J. B. Goodenough, Direct Cation-Cation Interactions in Several Oxides, *Phys. Rev.*, 1960, **117**, 1442–1451.

126 J. Kanamori, Superexchange interaction and symmetry properties of electron orbitals, *J. Phys. Chem. Solids*, 1959, **10**, 87–98.

127 P. Pokhilko and D. Zgid, Broken-symmetry self-consistent GW approach: Degree of spin contamination and evaluation of effective exchange couplings in solid antiferromagnets, *J. Chem. Phys.*, 2022, **157**, 144101.

128 P. Pokhilko and D. Zgid, Evaluation of Néel Temperatures from Fully Self-Consistent Broken-Symmetry GW and High-Temperature Expansion: Application to Cubic Transition-Metal Oxides, *J. Phys. Chem. Lett.*, 2023, **14**, 5777–5783.

129 A. V. Luzanov, A. A. Sukhorukov and V. E. Umanskii, Application of transition density matrix for analysis of excited states, *Theor. Exp. Chem.*, 1976, **10**, 354–361.

130 A. V. Luzanov and V. F. Pedash, Interpretation of excited states using charge-transfer number, *Theor. Exp. Chem.*, 1979, **15**, 338–341.

131 R. L. Martin, Natural transition orbitals, *J. Phys. Chem. A*, 2003, **118**, 4775–4777.

132 M. G. Delcey, L. Freitag, T. B. Pedersen, F. Aquilante, R. Lindh and L. González, Analytical gradients of complete active space self-consistent field energies using Cholesky decomposition: Geometry optimization and spin-state energetics of a ruthenium nitrosyl complex, *J. Chem. Phys.*, 2014, **140**, 174103.

133 D. S. Eggleston, K. A. Goldsby, D. J. Hodgson and T. J. Meyer, Structural variations induced by changes in oxidation state and their role in electron transfer. Crystal and molecular structures of *cis*-$[Ru(bpy)_2Cl_2]\cdot 3.5H_2O$ and *cis*-$[Ru(bpy)_2Cl_2]Cl\cdot 2H_2O$, *Inorg. Chem.*, 1985, **24**, 4573–4580.

134 C. M. Che, V. W. W. Yam and T. C. W. Mak, A novel monooxoruthenium(V) complex containing a polydentate pyridyl amine ligand. Syntheses, reactivities, and x-ray crystal structure of $[Ru^{III}(N_4O)(H_2O)](ClO_4)_2$, *J. Am. Chem. Soc.*, 1990, **112**, 2284–2291.

135 B. Durham, S. R. Wilson, D. J. Hodgson and T. J. Meyer, *Cis-trans* photoisomerization in $Ru(bpy)_2(OH_2)^{2+}$. Crystal structure of *trans*-$[Ru(bpy)_2(OH_2)(OH)](ClO_4)_2$, *J. Am. Chem. Soc.*, 1980, **102**, 600–607.

136 L. Lang and F. Neese, Spin-dependent properties in the framework of the dynamic correlation dressed complete active space method, *J. Chem. Phys.*, 2019, **150**, 104104.

137 J. C. Dobson and T. J. Meyer, Redox properties and ligand loss chemistry in aqua/hydroxo/oxo complexes derived from *cis*- and *trans*-$[(bpy)_2Ru^{II}(OH_2)_2]^{2+}$, *Inorg. Chem.*, 1988, **27**, 3283–3291.

138 D. E. Polyansky, J. T. Muckerman, J. Rochford, R. Zong, R. P. Thummel and E. Fujita, Water Oxidation by a Mononuclear Ruthenium Catalyst: Characterization of the Intermediates, *J. Am. Chem. Soc.*, 2011, **133**, 14649–14665.

139 J. J. Concepcion, M.-K. Tsai, J. T. Muckerman and T. J. Meyer, Mechanism of Water Oxidation by Single-Site Ruthenium Complex Catalysts, *J. Am. Chem. Soc.*, 2010, **132**, 1545–1557.